ABSTRACT

Title of Dissertation:	STABILITY AND SCALING OF NEURONAL AVALANCHES AND THEIR RELATIONSHIP TO NEURONAL OSCILLATIONS
	Stephanie Regina Miller, Doctor of Philosophy, 2019
Dissertation directed by:	Professor Rajarshi Roy, Institute for Physical Science and Technology
	Dr. Dietmar Plenz, National Institutes of Health

The generation of cortical dynamics in awake mammals is not yet fully understood. However, it is known that neurons leverage distinct organizational schemes to achieve behavior and cognitive function, and that this precise spatiotemporal organization may go awry in illness. In 2003, a form of scale-free synchrony termed “neuronal avalanches” was first observed by Beggs & Plenz in cultured cortical tissue and later confirmed in rodents, nonhuman primates, and humans. In this dissertation, we draw from monkey and rodent studies to demonstrate that neuronal avalanches capture key features of neural population activity and constitute a robust and stable (e.g. self-organized) indicator of balanced excitation and inhibition in cortical networks. We also show for the first time that neuronal avalanches and oscillations coexist in frontal cortex of nonhuman primates and identify the avalanche temporal

shape as a biomarker predicated upon critical systems theory. Finally, we present progress towards characterizing altered avalanche dynamics in a developmental mouse model for schizophrenia using 2-photon calcium imaging in awake animals

STABILITY AND SCALING OF NEURONAL AVALANCHES AND THEIR RELATIONSHIP TO NEURONAL OSCILLATIONS

by

Stephanie Regina Miller

Dissertation submitted to the Faculty of the Graduate School of the
University of Maryland, College Park, in partial fulfillment
of the requirements for the degree of
Doctor of Philosophy
2019

Advisory Committee:
  Professor Rajarshi Roy, Chair
  Professor Michelle Girvan
  Professor Chris Jarzynski (Dean's Representative)
  Professor Wolfgang Losert
  Dr. Dietmar Plenz

Acknowledgements

I am grateful for generous training and support received throughout my graduate career from innumerable colleagues, faculty, and staff members at the National Institute of Mental Health and the University of Maryland College Park. I owe particular gratitude to the UMD Chemistry Department's Dolphus E. Milligan Fellowship and to the UMD/NIMH IRTA Graduate Partnership Program for funding support that made this research and degree possible.

Special thanks to David Godlove at the NIH High Performance Computing Core for assistance navigating supercomputer resources, to Dave Ide at the NIH Section on Instrumentation for creation of equipment, to Craig Stewart for keeping the Plenz Lab stocked, and to my excellent post-bacc assistant, Samhita "Diya" Sengupta, UMD'18.

Many thanks to my undergraduate professors at Mount Holyoke College, especially Prof. W. Donald Cotter, whose courses in Inorganic Chemistry and in Science, Revolution, and Modernity greatly informed my fledgling scientific intuition. Thank you also to my previous research advisors: Prof. Bret Jackson at the University of Massachusetts Amherst, Dr. Richard Quinn at the SETI Institute, and Dr. Marc Cicerone at NIST.

Thank you to my father for leaving a copy of James Gleick's *Chaos* around the house, and to my mother, who listened to me talk through this dissertation and occasionally took dictation.

Finally, thank you most of all to my trifecta of mentors, Drs. Plenz, Roy, and Losert.

Table of Contents

List of Tables

List of Figures

Chapter 1: Introduction

There is a need for a qualitative leap in the development of medical interventions for brain health. Traditional psychiatric and neurological approaches to diagnosis and treatment may limit patient prognosis, especially patients with mental illness (3). Although there have been significant advances in neurological treatments, for example the development of deep brain stimulation (DBS) to treat Parkinson's disease (4), this progress has not been mirrored in treatment of psychiatric disorders (3). In order to innovate methods for restoring and maintaining a full spectrum of brain health, fundamental and translational neuroscience fields must join to develop integrated frameworks. A candidate integrated framework that will feature prominently in this dissertation is **critical brain dynamics**, which describes scale-free neuronal activity cascades in neocortex, the outermost region of the mammalian brain.

Neocortex tissue has a laminar structure wherein six descending layers serve distinct circuit functions. It was observed by Beggs & Plenz in 2003 that neuronal cell populations in superficial layer II/III exhibit signatures of self-organized criticality, a type of collective behavior characterized by large fluctuations and high complexity. This seminal discovery provided the first experimental evidence for **neuronal avalanches**, which are spatiotemporal cascades of action potentials that propagate akin to a branching process (5). In cortex, balanced yet non-equilibrium cascades unfold on a vast, reticular terrain of excitatory (glutamatergic) and inhibitory (GABAergic) synaptic networks. In this highly clustered neural environment (1), information is manifest in both biochemical structure and electrochemical dynamics (Fig. 1.1).

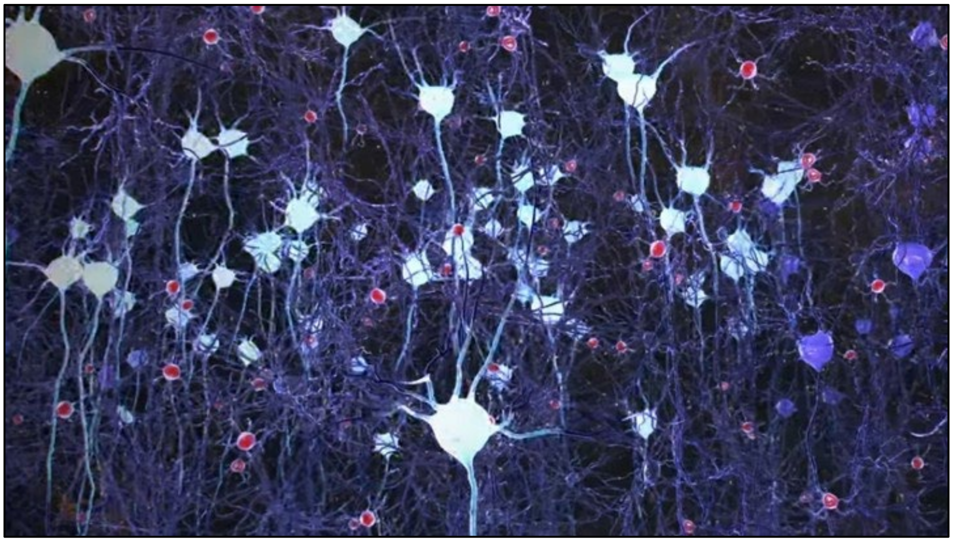

MIT PICOWER INSTITUTE FOR LEARNING AND MEMORY

Figure 1.1: Illustration of a neuronal neighborhood in cortex. A slightly stylized neighborhood of excitatory pyramidal cells shown resting (*blue*) and spiking (*white*). Neuronal dendrites branch upwards towards superficial layers and axons project downwards to deliver impulses locally or globally. Glial support cells are shown in red.

Here, we produce research characterizing neuronal avalanche dynamics in micro-scale (~500 μm^2) and meso-scale (~4 mm^2) neural populations in superficial layer II/III of awake mice and nonhuman primates. We combine avalanche analysis and network-based approaches to interrogate neural population activity through the lens of critical systems theory, revealing how neuronal avalanches unfold in time. We conclude with preliminary results from a study on altered cortical dynamics in schizophrenia-model mice. Throughout this dissertation, special attention is paid to how avalanche measures may become transiently modulated in spontaneous activity or permanently distorted in disease.

1.1 Neuronal signaling in cortical layer II/III

A single neuron is classically depicted as a spherical soma (the cell "body") with branching dendrites ("ears") extending upwards and a single axonal process ("voice") extending downwards. Many morphological variations are possible: dendrites may cluster around the cell soma, and axons can project locally or to other brain areas. Regardless of morphology, the principle feature of a neuron is that it fires **action potentials**, or "spikes", in which axonal "voices" transmit discrete electrochemical impulses to the dendritic "ears" of postsynaptic cells.

In a typical spike event, dendritic ion channels are pre-synaptically driven to permit afflux of positive e.g. sodium ions, which are normally kept at a high chemical gradient by ATP-powered Na^+/K^+ pumps. This inward Na^+ migration may raise the capacitance across the cell membrane from resting potential (~ -70 mV) to the spiking threshold (~ -50 mV), triggering a highly stereotyped kinetic process. Following sufficient excitatory postsynaptic potentials (ESPS), somatic voltage-gated channels open and the Na^+ permeability increases by 500-fold. Sodium ions flood down the electrochemical gradient, 'spiking' the membrane potential to +30 mV and triggering the release of the action potential down the axonal segment. Once an action potential reaches the axon terminal, voltage-gated calcium channels open and locally increased $[Ca^{2+}]_i$ allows neurotransmitter-bearing readily-releasable vesicles (RRVs) to release their contents into the synaptic cleft. Signaling molecules then diffuse ~20 nm to cross the cleft and bind to postsynaptic transmembrane receptors. Meanwhile, somatic ion channels open to permit K^+, Ca^{2+}, and Cl^- to cross the cell membrane on a refractory timecourse that, combined with active ion and proton pumps, returns the membrane potential to resting state within ~10 ms.

Importantly, any single neuron will synaptically release only one type of neurotransmitter; however, a broad variety of receptors can cause differential effects on the postsynaptic cell. From the viewpoint of systems neuroscience, the most important distinction between neuronal cell types is the type of neurotransmitter released. This dissertation focuses on two important signaling agents: the excitatory neurotransmitter **glutamate** and the inhibitory transmitter **γ-aminobutyric acid (GABA)**.

1.2 Population dynamics and neuronal oscillations

When considering the persuasiveness of a single synaptic impulse at influencing postsynaptic spike timing, the size of the synapse and its proximity to the base of the downstream axonal segment are important factors. Although most synapses are established on dendrites, the predominant GABAergic cell type, paravalbumin-expressing (PV) interneurons, will characteristically synapse directly onto the cell soma of downstream pyramidal (PYR) excitatory cells. The proximity of these synapses to the axon hillock, where action potentials are generated, can effectively "short circuit" even an imminent PYR spike. This strategic location, combined with the fast-spiking nature of PV interneurons, makes this cell type particularly persuasive in cortical brain dynamics. Indeed, PV interneurons are known to synchronize broad excitatory cell populations on a ~2-3 ms time delay in the synergistic perpetuation of a 30-50 Hz "gamma oscillation". Via this and similar feedback mechanisms (6), inhibitory and excitatory cells coordinate to form **neuronal oscillations**, wherein different cells types have distinct roles in the propagation of precisely timed spiking patterns by neuronal ensembles (7).

In mammals, there are multiple distinct physiological frequency bands essentially conserved across species (8). Spanning 0.5 - 130 Hz, these wave bands and their interactions (i.e. phase-amplitude coupling (9)) are associated with different cognitive states (i.e. slow delta waves during sleep (10)). In Macaque monkeys, nested theta-gamma waves may co-occur during ongoing brain activity (11, 12), and beta and gamma waves were anti-correlated during an *n*-back memory task (13). While considerable research has been produced on the role of neuronal oscillations in sensory processing, behavior, and cognition, their generating mechanisms are to a great extent still unknown.

The coordination of excitatory and inhibitory neurons is central to the temporal precision required for healthy brain function, and the intricate synaptic networks supporting precise temporal dynamics in the brain evolve throughout life. Certain periods during development are associated with pronounced vulnerability, and insults to e.g. neonatal brain may result in permanent deformation of cortical circuits.

1.3 Conceptual dualisms for describing neural synchrony

At the level of single cells, two simple methods for interpreting neuronal activity are rate coding, and alternatively, temporal coding. In a purely rate coding Poisson-spiking cell, it is not the precise moment that a cell spikes that matters, but rather how many spikes it generates in a given period of time. This is in contrast to the temporal code observed in spike-timing dependent plasticity (STDP). Although these two concepts stand somewhat at odds, the brain has been shown to leverage both schemes (14).

Emergent collective behaviors at the population level such as brain waves and neuronal avalanches can also be contrasted. In a neuronal oscillation, many cells regularly fire in concert within a specific frequency band to form a briefly deterministic activity pattern among participating cells (8, 15). This type of synchrony is distinct from neuronal avalanche dynamics. During avalanching, cells fire according to a stochastic domino-effect and cascades are organized into clusters displaying statistical signatures of self-organized criticality (16). In Chapter 3 we will find that large groups of neurons can flexibly switch between oscillations and avalanches, maintaining signatures of both (17, 18).

Two prominent frameworks for describing the macroscopic organization of neuronal activity are ‘top-down’ and ‘bottom-up’ processes. A top-down approach centers the interaction of a subject and the environment in the context of goals and learned rules. In this framing, neurons coordinate for the purpose of achieving sensory integration and outputting appropriate behavioral actions. From the perspective of bottom-up control, brain cells coordinate because they are subject to a variety of spontaneous and evoked molecular forces serving to either promote or suppress the emission of action potentials. However, the top-down/bottom-up dichotomy has failed to explain some phenomena (19), and there is need for a neuroscientific framework capable of integrating goal-directed influences with physically salient signals, a framework which is not conceptually dependent upon a separation of scales.

1.4 Neuronal avalanches and the awake state

Neuronal avalanches were first discovered in cascades of cortical activity in organotypically cultured *in vitro* preparations (5). In the following years, avalanche dynamics were confirmed in anesthetized rodents (2, 16, 20) and cats (21), and in awake rodents (22) and nonhuman primates (2, 23). In humans, avalanches have been observed in many conditions including the awake state (24-26), anesthesia (27), and illness (28-31).

Critical brain dynamics can be conceptualized on the following heuristic level: if the canonical definition of healthy cortical activity is critical dynamics, then the subcritical absorbing state (32) might be considered analogous to a coma, while supercritical cortical activity has been associated with the epileptic regime (28) (but see (33) for discussion of subcritical or near-critical dynamics as the healthy resting state of the brain). The current body of literature indicates that neural dynamics are transiently moved away from avalanche structure into other types of synchrony during evoked activity and behavior(13), then return to avalanching afterwards (23). We may therefore infer that the structure of spontaneous brain activity in healthy mammals is described by avalanches unfolding at or in close proximity to a phase transition.

1.5 Quantifying neuronal avalanches

There are certain common expressions for quantifying bursting events in critical systems. The magnitude or size, S, of an avalanche is defined as the number of activations occurring over the course of a single cascade, and the size probability distribution $P(S)$ is theoretically described by a power law with critical exponent α,

$$P(S) = S^{-\alpha}. \tag{1.1}$$

The avalanche duration distribution follows the power law,

$$P(L) = L^{-\beta}, \tag{1.2}$$

where the lifetime *L* is equal to the total duration *T* of a cascade divided by the temporal resolution Δt, such that *L* = *T*/Δt. The time bin width Δt is empirically provided by the sampling frequency, the frame rate, or the average inter-event-interval <*IEI*> (34). The mean-size-per-duration distribution is described by yet another power law,

$$\langle S\rangle(L) = L^{\frac{1}{\sigma\upsilon z}}, \tag{1.3}$$

where the critical exponent $\frac{1}{\sigma\upsilon z}$ captures how cascade magnitude scales with the temporal length of the burst of neural activations. We also find that the precise profile of activations over the course of a cascade, $s(t, L)$, is an interesting measure. Critical systems theory predicts that avalanche shapes are scale-invariant and thus obey the shape collapse function,

$$\langle s\rangle(t, L) = L^{1-\frac{1}{\sigma\upsilon z}} * \mathcal{F}\left(\frac{t}{L}\right).$$

(1.4)

$\mathcal{F}$ represents the characteristic burst shape in time, the average of which is expected to be an inverted parabola (35).

This final expression is derived from renormalization group theory, developed in part by Wilson (36) and Fisher (37). Renormalization is the process of "collapsing" complexity onto a single axis to capture how models change across scales. If collective behavior is scale-invariant then the mathematical description of the dynamics is known as the **universality class**. For neuronal avalanches, the universality class is thought to be directed percolation. In high dimensional (≥ 4D) systems such as the brain, this universality class is associated with the following critical exponent values: $\alpha = 3/2$, $\beta = 2$, and $\frac{1}{\sigma v z} = 2$ (38). Furthermore, critical systems theory predicts certain critical exponent relations including $\frac{\beta-1}{\alpha-1} = \frac{1}{\sigma v z}$. This relation and the above predictions (Equations 1 - 4) can be tested independently and against each other in both simulated and real brain.

1.6 Modeling critical brain dynamics

In the interest of developing a robust theoretical framework, as well as sparing unnecessary animal research, it is useful to study avalanching neuronal networks *in silico*. Critical phenomena in extended systems have classically been studied in physical and geophysical models such as the critical branching model (39), the Bak-Tang-Wiesenfeld sandpile model (17), and the Ising model of ferromagnetism (40). Early descriptions of propagating neuronal activity as a critical branching process were explicitly published by Per Bak (41), and were complemented and further elaborated on by a series of model studies (42-45). In these models, the critical branching parameter, σ, defined as the average ratio of the number of descendants to ancestors within a cascade, captures the balance between stable propagation (σ=1), explosive activity (σ>1), and signal die-out (σ<1). The first experimental demonstration of cortical activity propagating in the form of a critical branching process, giving rise to the term ‘neuronal avalanches’, was reported by Beggs and Plenz (5). In recent years, dynamical and biophysical models have produced increasingly realistic neuronal avalanche dynamics. These include the Human Brain Project's large-scale biophysical model (46), the Landau-Ginzburg model (32), and the critical oscillator (CROS) model (47).

For empirical scientists, it is important to fit a robust statistical model to the distribution of real data (48) and thus refine the generation of simulated data with similar statistical qualities as measurements made *in vivo* or *in vitro*. With regard to the generalizability of neuronal avalanche research, we note that neuronal interactions determine the dynamics and universality class, not the features of individual cells. The broad range of avalanching systems found in nature suggests the possible utility of neuronal avalanche theory for research in other fields such as neuromorphic engineering and brain-computer interface development.

1.7 Neurological and mental health applications

When considering the many levels of neuronal dynamics, it is important to note that malfunction on any level may percolate to other scales, causing dynamical and/or structural maladaptations. In part, this intricacy represents an obstacle; disentangling the effects of some initial source of dysfunction is especially challenging in recurrent systems. However, such a broad spatiotemporal character may also afford many potential angles from which to probe the nature of a pathology, resulting in a richer description of healthy function and mechanisms of illness.

A new neuroscientific framework which captures the brain's complexity and chimeric capacity (a.k.a. supporting metastability and flexible switching between dynamic states) could be advantageous for translational research. Neuronal avalanche research may provide additional and complementary measures of the effects of established pharmacological treatments which are not completely characterized in their mechanisms of action or full breadth of effect. Further, avalanche measures hold notable potential as new biomarkers with diagnostic and prognostic value; in Chapter 3, we present avalanche shape trends as a candidate biomarker.

New dynamical biomarkers may have considerable import for the science of mental health. For example, it is known that gamma waves are reduced in amplitude and coherence in the brains of people with schizophrenia (49). By identifying simultaneous changes in avalanche organization, it may be possible i) to implicate specific cell types or dynamical states as the source of pathology, and ii) to identify how those circuit components are rescued in treatment. A second example is the connection between epilepsy (29) and sleep deprivation (24, 28). Recent research on critical slowing down in the cortex of epileptic patients (50) has revealed that the loss of sleep-facilitated neuronal network normalization can render an already trending-towards-supercritical brain even more susceptible to system-wide events e.g. seizures (51). Other pathological conditions where neuronal avalanches have been investigated include premature (30) and hypoxic birth (31).

1.8 Dissertation outline

In this dissertation, we experimentally explore the applicability of critical systems theory to neural dynamics in cortex of monkeys and mice with implications for human neuroscience. Leveraging electrophysiology, calcium imaging and optogenetics, as well as behavioral testing and neural network analysis, we confirm previous observations that superficial cortex operates close to a critical state in a stable manner over days and weeks, and, importantly, we find that testing the scale-invariance of avalanche temporal shape reveals the precise structure of spontaneous neuronal oscillations across timescales. We also investigate whether brain disease can be characterized by aberrant excitation/inhibition balance and disorganized population synchrony, following up on a recent study in a rodent model of schizophrenia which found that population bursting showed deviations from critical dynamics (20). Ultimately, the results of this dissertation suggest that critical systems theory is likely to offer valuable improvements to traditional neuroscientific practice.

In Chapter 2, cortical network structure and dynamics *in vivo* are investigated over long timescales e.g. many weeks. We establish that local field potentials in awake nonhuman primates display avalanche dynamics in a stable manner over up to 73 days despite fluctuating individual pairwise electrode correlations. We also implement a Normalized Count network reconstruction to remove the influence of common input and confirm previous findings of an integrative, clustered functional network upon which neuronal avalanches unfold.

In Chapter 3, we build upon the Chapter 2 finding of stability of critical brain dynamics over time, leveraging our full nonhuman primate data volume to attain precise statistics on even large and rare cascades. Testing predictions from critical systems theory (35) and an *in vitro* study suggesting that avalanche shapes are scale-free (52), we apply the renormalization shape collapse function to determine whether avalanches *in vivo* display scale-invariant profiles at timescales impacted by spontaneous oscillatory bursts.

In Chapter 4, we present preliminary data towards detecting aberrant avalanche and network dynamics in a developmental mouse model for schizophrenia. This study, motivated by a need to identify the role of cell-type specific cortical circuit components in maintaining healthy brain activity, investigates the contribution of PV, SST, and VIP interneurons to coordination and synchrony among excitatory principle cells. By combining behavioral assays of episodic memory with multi-photon calcium imaging and optogenetic stimulation in PV-, SST-, and VIP-Cre transgenic mouse lines, we present initial findings pointing to impaired episodic memory and deviations from criticality in neuronal activity of PCP-treated mice. The eventual goal of this work is to characterize the breakdown of precisely coordinated activity in cortical layer II/III, the seat of cognition and critical brain dynamics.

Chapter 2: Stable avalanche dynamics and integrative network properties in nonhuman primates

This Chapter is adapted from research in preparation for submission. Nonhuman primate data was collected by Dr. Shan Yu.

The brain must balance stability over time with the need for flexibility and learning. Much research has focused on understanding how individual synapses and circuits change and evolve during cortical activity, yet little is known about which network and dynamical properties are preserved as required for stable functioning. In this Chapter, we specifically study "friendship networks" (characterized by high neighborhood overlap between strongly connected nodes), which have been observed in the functional connectivities of many complex networks including cortex. We identify several stable global network and activity characteristics in awake Macaque monkeys. These network properties were observed alongside robust avalanche dynamics despite fluctuating functional connections between cortical sites, suggesting that ongoing synaptic and functional reorganization preserves the connectivity balance and maintains avalanche dynamics.

2.1 Introduction

Neuronal networks must function robustly and reliably even while their internal configurations change to flexibly adapt to e.g. environmental challenges. Such changes in internal configurations are typically found at the synaptic level, i.e. individual connections between neurons, or at the property of single neurons, e.g. their ion channel composition. Research in invertebrates has established that those changes can often be profound yet maintain essential network dynamics, such as oscillations for digestive functioning (53). For mammals, and in particular within the cerebral cortex, this balance between stability and flexibility has been largely addressed in the context of neuronal spiking activity (for review see e.g. (54)), where it was found that activity remains heterogenous across the population and over time despite functional changes e.g. with respect to sensory tuning cures. The dynamical state that might give rise to such stable heterogeneity, however, is much less understood, nor is it known the extent to which configurational changes networks might be allowed while maintaining such heterogeneity.

Heterogeneous activity in the form of neuronal avalanches has been the hallmark of ongoing (5, 22) and evoked brain activity (23, 55) in superficial layers of the cerebral cortex. Avalanches reflect spatiotemporal clusters of activity that exhibit power law distributions in cluster size and duration (22, 28) supporting the idea that the cortex operates close to a critical state (56-60). The scale-invariant hallmark of avalanches has been found to capture ongoing pyramidal neuron group activity *in vivo* at the microcircuit scale (22, 61) as well as neuronal activity in nonhuman primates at the mesoscopic level, i.e. the local field potential (LFP) (2, 16, 23, 55, 62). In human, similarly macroscopic activity was measured in electroencephalography (EEG; (24)), magnetoencephalography (MEG; (25)), and functional magnetic resonance imaging (fMRI; (63, 64)). While *in vitro* studies demonstrated the emergence of neuronal avalanches early during development when superficial layers develop (65, 66), the robustness of avalanche dynamics over many weeks in the adult brain *in vivo* has not been quantified. Furthermore, avalanche dynamics have been found to exhibit a functional connectivity that is small-world, specifically with an integrative “friendship” organization, wherein nodes with strong connections are likely to have many common neighbors (1, 67).

Here we examine the stability of neuronal avalanches and the underlying functional connectivity over many weeks in the brain of nonhuman primates. We quantify the power law distributions of avalanche dynamics and the entropy of the mixing of link distributions over time for both pairwise correlation networks and directed causal networks. We find that neuronal avalanche markers as well as functional connectivity in both prefrontal and premotor cortex of monkeys are highly stable over many weeks.

2.2 Methods

2.2.1 Animal procedures

All animal procedures were conducted in accordance with NIH guidelines and were approved by the Animal Care and User Committee of the National Institute of Mental Health (NIMH; Protocol LSN-11). Three adult nonhuman primates (NHP; *Macaca mulatta*; 1 male, 2 females; 7–8 years old) received two chronic implantations of high-density 96-microelectrode arrays (Blackrock Microsystems; 4×4 mm^2; 400 µm interelectrode distance; 10×10 grid with corner grounds). To direct recordings towards superficial cortical layer II/III, electrode shanks of 0.6 mm length were used in prefrontal cortex (PF; $n = 4$), and shanks of 1 mm length were used for premotor cortex (PM; $n = 2$). During recording sessions monkeys sat head-fixed and alert in a monkey chair with no behavioral task given. Portions of this dataset have been analyzed previously (2, 24, 60).

2.2.2 Local field potential recordings in awake monkeys

Simultaneous and continuous extracellular recordings were obtained for 12 – 60 min per recording session (2 kHz sampling frequency), band-pass filtered between 1 – 100 Hz (6th-order Butterworth filter) to obtain the local field potential (LFP), and notch-filtered (60 Hz) to remove line noise. About 2 ± 1% of time periods were removed from functional electrodes due to artifacts introduced by e.g. vocalization, chewing, sudden movements. These artifacts were identified by threshold crossing (SD > 7) and excised (± 0.25 s). Arrays on average contained 86 ± 8 functional electrodes that exhibited 64 ± 50 μV of spontaneous LFP fluctuations (SD). Channels which had been removed from any recording were discounted for all recordings. Electrode LFPs were z-transformed and recording sessions for each array were analyzed individually. The current study represents a combined 26 hr of ongoing cortical LFP activity.

2.2.3 Avalanche definition

For each electrode in the array, absolute peak amplitudes and times of negative LFP (nLFP) threshold crossings (–2 s.d.) were extracted at the temporal resolution Δt (set to the average inter-event interval, $<IEI>$ = ~3 ms) and combined into a matrix, i.e. raster, with rows representing electrodes and columns representing time steps. Based on a population time vector, obtained by summing nLFPs in the raster for each time step, avalanches were defined as spatiotemporal continuous activity on the array bracketed by at least one time bin of no activity. The size of an avalanche, S, was defined as the number of nLFPs participating. Scale invariance of S was visualized by plotting probability distributions $P(S)$ in double-log coordinates.

2.2.4 Avalanche statistical tests and slope estimates

The maximum log-likelihood ratio (LLR) was calculated to test potential power law distributions against the alternatives of exponential or log-normal distribution models (16, 48). Slope estimations were based on the linear regression of log converted data excluding lower and higher cut-off regions. To determine α, we used the range of S = 1 to 40, which excludes the distribution cut-off close to the total number of functional electrodes on the array (n = >70).

2.2.5 Normalized Count network reconstruction

To remove the influence of shared input to electrodes on the array which inflates the Pearson's pairwise correlation, we conducted a network reconstruction. This nonparametric method, called the Normalized Count (NC) approach, began by setting uniform prior link probabilities, then finding the posterior probabilities for all nodes n_a which were active in the preceding time bin Δt. The time bin width was set to the average inter-event interval $<IEI>$, ~3 ms. Pairwise shuffling was implemented to account for noise. Advantages of NC approach over comparable methods, such as Iterated Bayesian or Single Source methods, have been enumerated in (68) and include superior computational efficiency and accuracy of reconstruction in the presence of noise, which are important considerations for analysis of large LFP time series collected in awake *in vivo* preparations.

2.2.6 Network analysis

Network analysis was conducted for each recording session individually. Pairwise correlation networks were pruned before clustering analysis and diagonal elements were removed. Rather than applying a strict minimum R threshold for pruning, which would leave our analysis vulnerable to inter-subject differences in electrode impedances, etc., we instead sequentially removed weakest links in 0.01 increments until a predefined sparsity of 40% was achieved. Weight bins were divided into deciles and quintiles for ease of visualization (Fig. 2.4, 2.5).

The clustering coefficient C_{Lij} was defined as the ratio of common neighbors to all neighbors. In an integrative network, there is a positive correlation R_{CL} between clustering C_{Lij} and weight w_{ij} such that strongly connected nodes are likely to share many common neighbors. Link-pruning analysis of excess clustering ΔC was controlled via degree sequence preserved randomization (DSPR) (1).

2.2.7 Network link mixing and entropy analysis

Fluctuations in link weights varied with time in both pairwise correlation and directed causal networks (Fig. 2.4). To visualize fluctuations in link strengths, links were grouped into quintiles and dispersion over days was shown as increasing overlap between colored-shaded areas. To determine whether link fluctuations were cumulative, we calculated the entropy of the distributions over successive recordings. Because all successive distributions were measured relative to Day 1, entropy measures were plotted beginning at the second recording for each subject.

2.3 Results

Chronically implanted high-density microelectrode arrays were used to monitor ongoing local field potential activity (LFP; 1 – 100 Hz) in premotor (PM, $n = 2$ arrays) and prefrontal cortex (PF, $n = 4$ arrays) of three nonhuman primates (*Macaca mulatta*; K, V, N) sitting in a monkey chair. The animals were awake during the recording sessions but were not given any specific stimulus or task. About 4 ± 2 hr of activity were analyzed during 9 ± 7 recording sessions over the course of 5 ± 4 weeks (85 ± 8 electrodes/array).

2.3.1 Stability of average pairwise correlation over many weeks in prefrontal and premotor cortex

We began by describing local field potential fluctuations (LFP, 1-100 Hz, Fig. 2.1*A*). We found *1/f* scaling, a signature of temporal correlations, in the power frequency plot which also displayed oscillatory signatures characteristic of resting-state dynamics (Fig. 2.1*B*). We characterized array activity in terms of pairwise correlations and their distributions (Fig. 2.1*C, D*) and noted that the average correlation strength varied across arrays but was consistent over time within arrays (Fig. 2.1*E, F*).

2.3.2 Stability of the power law in avalanche sizes over many weeks

We next explored the distribution of neuronal avalanches, which reflect a critical balance between excitatory and inhibitory forces in the brain. Local array events were defined as sustained negative deflections in the LFP at each electrode (Fig. 2.2*A*). LFP events were clustered on the array. The probability density distribution of cluster sizes,

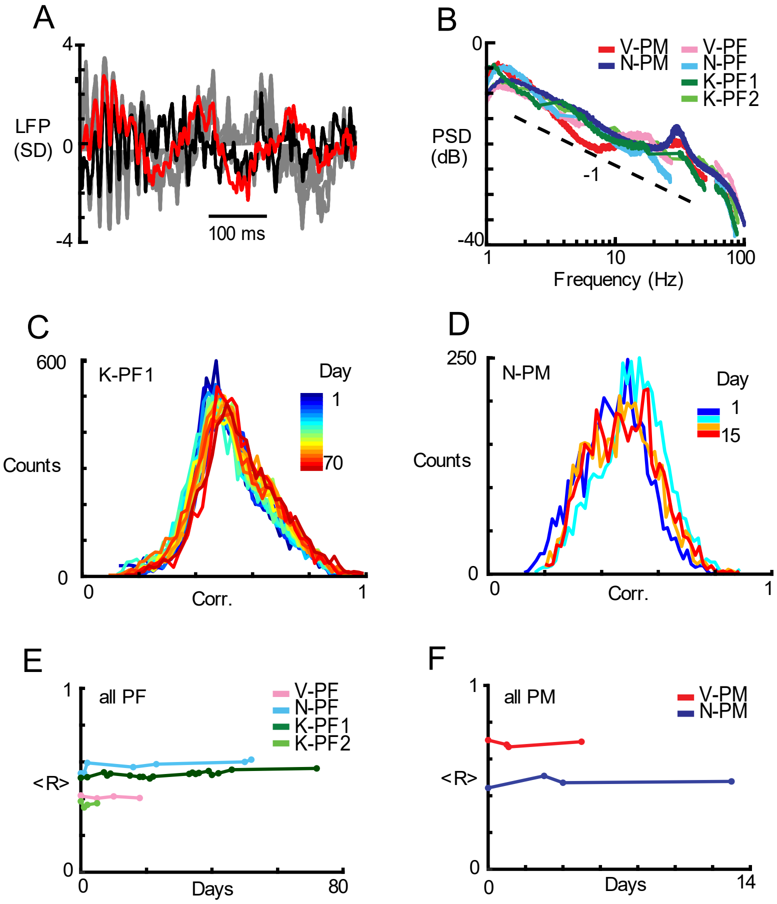

Figure 2.1: Pairwise and higher order correlations are stable over weeks in cortical layer II/III populations of NHP. ***A***, In superficial cortex of nonhuman primate (NHP), two example electrode local field potential (LFP) traces (*black, red*) exhibit complex behavior, in this case transient global synchrony followed by a period of independent fluctuations. ***B***, Power spectrum density (PSD) of the LFP with 1/*f* slope of -1 indicating the presence of broad temporal correlations (*color coded, average of single electrode PSDs*; *broken line*: 1/*f*). ***C, D***, Normalized histogram of pairwise correlations between all functioning channels for each recording day (*color bar*) in two subjects (*left*: prefrontal recording in NHP K; *right*: premotor recordings in NHP N). ***E, F***, The array-averaged correlation strength was stable over weeks in all prefrontal arrays (*left*) and in both premotor arrays (*right*).

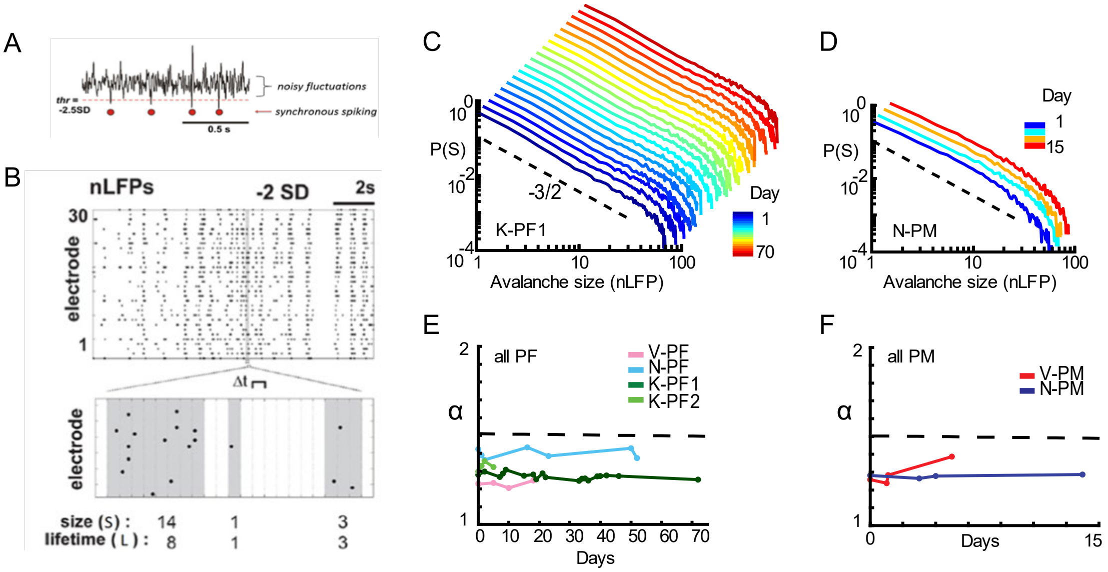

Figure 2.2: Signatures of neuronal avalanche dynamics are stable over weeks in cortical layer II/III populations of nonhuman primate. ***A***, Ongoing single electrode LFP with negative threshold crossing (2SD; *broken line*) defines nLFP times and peaks (*asterisks*). ***B***, Concatenating successive time bins with at least 1 nLFP defines nLFP clusters of size 14, 1, and 3 (*gray*) on a 32-electrode subsection of the array. ***C, D***, Power law in nLFP cluster sizes identifies avalanche dynamics for all recordings in two subjects ($\Delta t = \langle \mathrm{IEI} \rangle$). *Broken line*: power law with slope -3/2 *Color bar*: Recording day. Size distributions remain power laws for all days (LLR values > 0 significant; vs. exponential distribution. ***E, F***, Stability in slope α as a function of time (*color coded*).

which range from size 1 to system size, exhibited power laws demonstrating the presence of neuronal avalanches in all subjects, in both cortical areas, and on all recording days (Fig. 2.2*C, D*). Log-likelihood tests confirmed that for all recordings analyzed, avalanche size distributions were better fit by a truncated power law than an exponential ($p < 0.005$) or a log-normal distribution ($p < 0.005$). The robustness of the power law was associated with a consistent critical exponent α in line with theory (38) (Fig. 2.2*E,F*).

2.3.3 Stability of integrative global network properties and stable entropy mixing over many weeks

Next, we reconstructed functional networks using the Normalized Count method in order to reduce the influence of common input (Fig. 2.3). We found that functional network link strengths derived by this method distributed as an exponential over more than 3 orders of magnitude in link strength for a ~80 node network for all days (two subjects, Fig. 2.3*A, B*) and subjects (Fig. 2.3*C, D*).

In an integrative network, there is a positive correlation R_{CL} between C_{Lij} and w_{ij} such that strongly connected nodes are likely to share many common neighbors. Results of link-pruning analysis of excess clustering ΔC calculated via degree sequence preserved randomization (DSPR) (1) are shown in Figure 2.4. In cortical LFP networks, the clustering of common neighbors was high, and the clustering effect increased with link weight (Fig. 2.4*A, B*). Therefore, the correlation between excess clustering and link strength R_{CL} was found to be strongly positive and stable over time (Fig. 2.4*C, D*). Pruning of weak links had negligible effect on the network structure as evidenced by a linear trend in the excess clustering until the vast majority (80-90%, Fig. 2.4*E*, solid lines) of the links were removed. In contrast, top-pruning (*dotted lines*) resulted in an immediate decrease in clustering in a manner characteristic of integrative networks. This result was found consistently in all recordings for all subjects. The integrative clustering motif was robust to weak-link-pruning, whereas the clustering 'backbone' of the network quickly degraded when strong links were pruned. The measure of

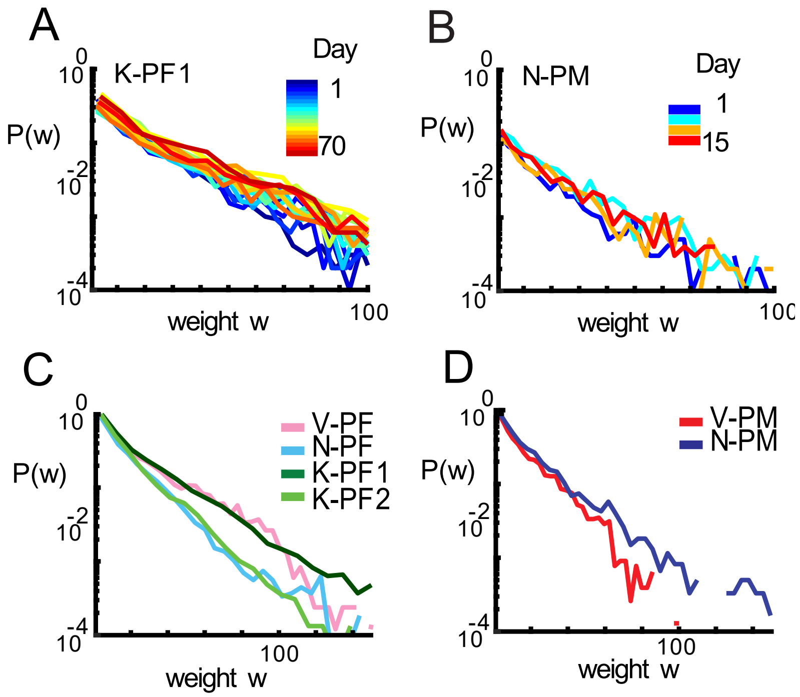

Figure 2.3: Reconstructed link strength on the electrode array network consistently distributes as an exponential. In prefrontal (***A*****,** K-PF1) and premotor (Nom-PM, ***B***) cortex of nonhuman primates, the Normalized Count reconstruction extracted directed link strengths from the MEA network that distributed exponentially on all recording days (*color bar; all days*). ***C*****,** ***D*****,** Normalized probability distribution trends were consistent across areas and subjects (*color code*; *NHP-area*).

robustness to weak-link pruning, M, was larger than zero and was positively correlated with R_{CL} as described previously for ongoing activity in nonhuman primates (1).

In an extension of Figure 2.1*C, D* and Figure 2.3*C, D*, we show that pairwise correlations assigned to strength quintiles (Fig. 2.5*A, B*) showed mixing as increasing overlap between colored-shaded areas between Day 1 and the second recording, yet comparing the second recording and later days did not display further mixing (Fig.

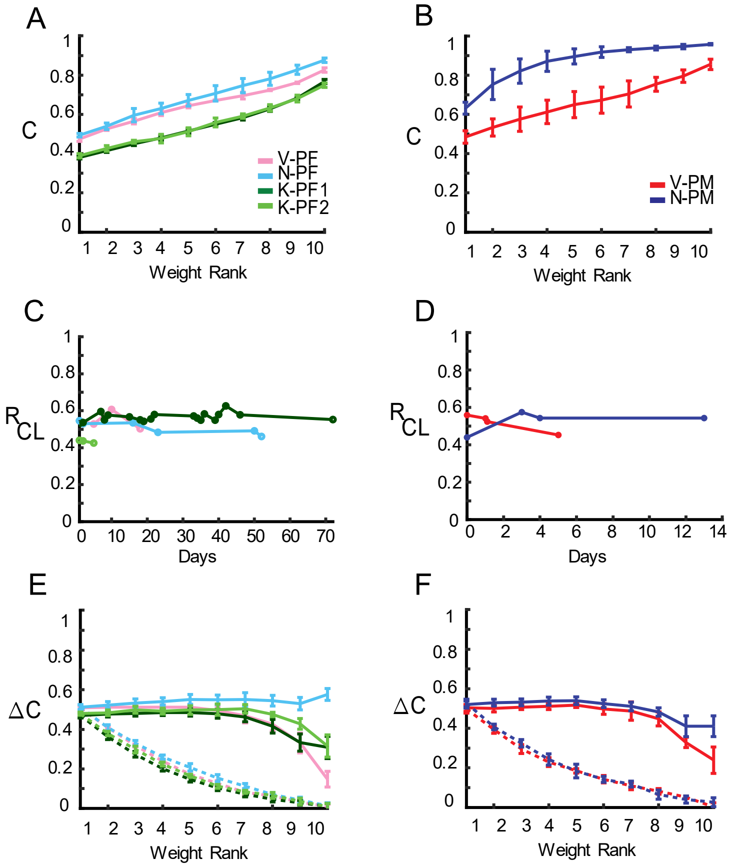

Figure 2.4: Link-clustering analysis reveals that integrative global network properties are stable over time. Clustering increased with link strength in all prefrontal (***A***) and premotor (***B***) cortical arrays (*color coded; NHP-area*). ***C, D,*** Analysis of cortical networks showed strongly positive R_{CL} over all recording sessions for up to 73 days. ***E, F,*** Link-pruning analysis of excess clustering ΔC calculated via degree sequence preserved randomization (DSPR) (1) showed that the integrative clustering motif was robust to weak-link-pruning (*solid lines; error bars denote mean ± SD over all recordings for an array*), while the clustering 'backbone' of the network quickly degraded when strong links were pruned first (*dotted lines; reverse weight rank on the lower axis; color coded*).

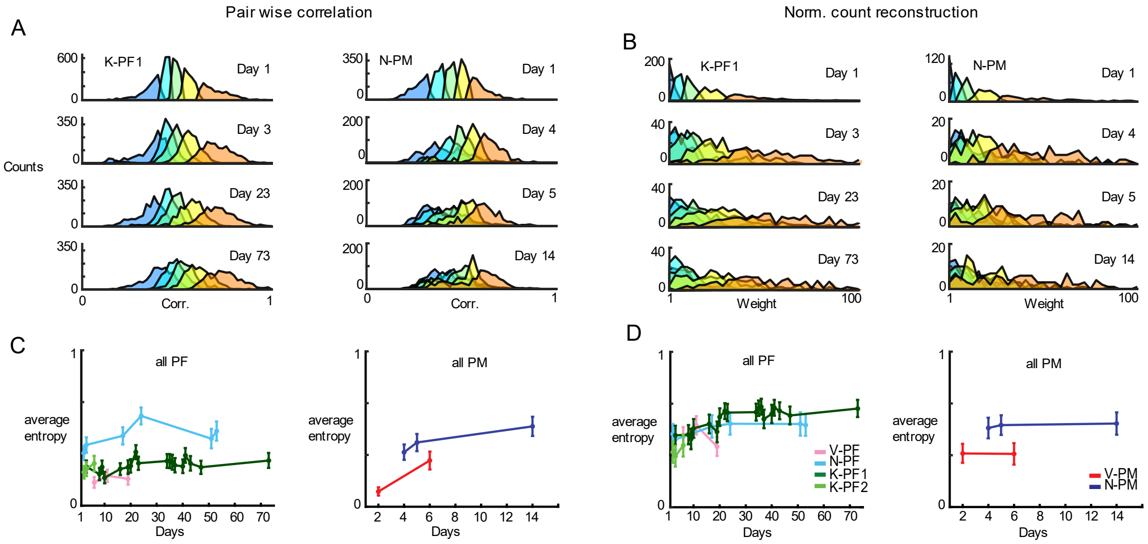

Figure 2.5: Network link weight fluctuation over days does not fundamentally alter weight distributions. ***A***, Pairwise correlations assigned to strength quintiles *(blue fill; weakest quintile; red fill; strongest quintile*) for one sample prefrontal array *(Ker-PF1, left*) and one premotor array (*Nom-PM, right*) show fluctuation-driven dispersion over days as increased overlap between colored-shaded areas. ***B***, Normalized Count (NC) reconstructed network link weights reveal the same trend. ***C, D***, Both pairwise correlation (***C***) and NC reconstructed (***D***) networks show a trend of stability in the entropy of mixing across arrays and subjects (*color code: NHP-area*).

2.5*C, D*). Normalized Count reconstructed network link weights revealed the same trend, and both pairwise correlation and NC reconstructed networks show a trend of stability in the entropy of mixing across arrays and subjects over days and weeks. This implies that although link weights fluctuated, they did not usually escape their weight rank, and fluctuations averaged to net zero as evidenced by a stable envelope of the distribution over all quintiles (c.f. Fig. 2.1*C, D*, Fig. 2.3*C, D*).

2.4 Discussion

Our results demonstrate that cortical networks conform to a small-world, integrative clustering motif upon which neuronal avalanche dynamics are stable over weeks. Measurements were made with two 10x10 microelectrode arrays implanted in premotor and prefrontal cortical areas for a total of 6 data sets across 3 nonhuman primate subjects. Neuronal avalanche analysis consistently produced power law distributions in avalanche sizes, and clustering analysis of pairwise correlations and reconstructed networks established that functional networks were strongly integrative ($R_{CL} > 0$) for all subjects and all arrays. Our findings are in line with previous research on network organization in cortex, including previous applications of the Normalized Count approach to neural populations (1). The stability of neuronal avalanches, link strength averages and distributions, and integrative network topology were demonstrated over time for both pairwise correlations and reconstructed causal networks.

Correlation-based network approaches are known to introduce spurious links and inflated correlations strengths due to common drive. The Normalized Count (NC) reconstruction of the underlying causal network provides an efficient approach for analyzing long time series from small and large networks and is effective at removing correlations from common input (68). Applications of the NC approach have indicated that integrative and small-world network organization is present in both *in vitro* (68) and *in vivo* (1). Note that empirically, the NC algorithm is capable of up to 5 orders of magnitude (at least regarding node initiation frequency), and with different LFP threshold, filter bounds, etc., more orders of magnitude might be achieved which would provide for a fine-grained estimation of link strengths (68).

Our analysis of weight bands demonstrated that individual link strengths do not show any particular trend over time. The entropy analysis showed dispersion of link weights for each band within a short period of time after initial experimental recordings and was stable thereafter. The initial dispersion might be attributed to the initialization of our measure but could also reflect instabilities during an early period of recovery from MEA-implantation surgery.

In conclusion, we found that although the specific synaptic terrain of the cortex is dynamic, macroscopic network properties and emergent population dynamics are robustly observed over days and weeks. We suggest that balanced changes in functional connectivity do not affect information transmission properties associated with avalanche dynamics, and that ongoing variation in precise link structure is constrained by the homeostatic maintenance of global integrative network properties. This work has implications for studies of network properties of the brain in e.g. autism and other disorders characterized by altered neurological development on the network and population level.

Chapter 3: Neuronal avalanche shapes reveal nested θ/γ-wave structure in resting monkeys

This Chapter is adapted from an article in peer-review. Nonhuman primate data was collected by Dr. Shan Yu.

The most common framework for understanding the temporal organization of brain activity is oscillations, or “brain waves”. In oscillations, distinct physiological frequencies emerge at well-defined temporal scales, dividing brain activity into time segments underlying cortex function. In this chapter we identify a fundamentally different temporal parsing of activity in cortex. Activity cascades are found in many complex systems. In the cortex, they arise in the form of neuronal avalanches which capture ongoing and evoked neuronal activities at many scales. The scale-invariant nature of avalanches suggests that the brain is in a critical state, yet predictions from critical theory on the temporal unfolding of avalanches have yet to be confirmed experimentally. In awake Macaque monkeys, we demonstrate the motif of an inverted parabola that governs the temporal unfolding of neuronal avalanches spanning up to hundreds of milliseconds. This symmetrical motif is scale-invariant, that is, it is not tied to time segments, and it exhibits a scaling exponent χ close to 2 in line with prediction from theory of critical systems, distinguishing generational models of neuronal avalanches from non-biological approaches. γ–oscillations transiently modify this parabola thereby providing a temporal segmentation to inherently scale-invariant, critical dynamics. Our results identify the co-existence of two principles of temporal organization in the brain, avalanches and oscillations, predictive of normal and pathological brain function.

3.1 Introduction

Cascades are found in many complex systems. The spreading of information in social media (69), the tracking of infections during epidemics (70), and the propagation of neuronal activity in the brain (5) are prominent examples of how cascades and cascade failures (13, 71-73) provide insight into system function. In the brain, cascading activity has been identified in the form of neuronal avalanches by the presence of power laws in the distributions of cascade size and duration (5, 62). The scale-invariant nature of neuronal avalanches describes the firing of nerve cells (22, 74) and, at larger scales, captures neuronal population dynamics in zebrafish (75), nonhuman primates (23, 55, 62), and humans (25, 28, 29, 63, 76, 77). This supports the idea that the brain might operate close to a critical state (78-81) where numerous aspects of information processing are optimized (29, 56-60, 82, 83). Yet, avalanche size and duration statistics do not provide insight into the process of cascading itself. This process can be more rigorously assessed by studying the temporal profile of avalanches, that is, how avalanches initiate locally, expand, and shrink in the brain as they evolve in time.

Theory (35, 84-86) predicts that cascade profiles follow an inverted parabola in critical systems, but it is currently not known whether such a unique avalanche profile guides brain activity. Variable and asymmetric profiles have been reported for neuronal cultures (87, 88) and profiles seem to depend on avalanche duration in humans (29). Identifying the correct profile of neuronal avalanches should be of particular importance given recent findings that profiles predict recovery from brain insults (30, 31) and can be used to distinguish between models of avalanche generation (52, 89-91).

A second prediction from critical systems theory is that the avalanche parabola can be collapsed over many avalanche durations with a scaling exponent χ (note that this is not the susceptibility χ, but instead the critical scaling exponent also called $1/\sigma\upsilon z$) larger than 1.5 (35, 84-86). Robust collapses, though, require a large amount of data to include long avalanches, which are rare. Equally challenging are recent reports that χ ranges between 1 – 1. 5 for rodent tissue *in vitro* (87, 88) and *in vivo* (61) as well as in human MEG (29), suggestive of non-critical dynamics (90). Scaling collapse was recently found for $\chi \cong 2$ in zebrafish whole brain activity (75), yet it is unknown whether this is the case in mammalian cortex. In the mammalian brain, profile estimates are in fact further challenged by the presence of prominent brain oscillations, such as gamma activity (γ; ~30 – 100 Hz) (8, 92, 93). Such oscillations establish temporal scales for neuronal dynamics that seem counterintuitive to a scale-invariant avalanche profile.

Here we reliably identify avalanche profiles at several temporal resolutions, 1- 30 ms, using long-term recordings from awake nonhuman primates with high-density microelectrode arrays. By overcoming statistical and oscillation-induced constraints in profile collapse, we show that neuronal avalanches exhibit the profile of an inverted parabola with a scaling exponent $\chi \cong 2$ as predicted for critical dynamics. Our findings suggest a novel scale-invariant temporal motif that governs neuronal activity in cortex over many durations to which oscillations add a distinct regularity in time.

3.2 Methods

3.2.1 Animal procedure

All animal procedures were conducted in accordance with NIH guidelines and were approved by the Animal Care and User Committee of the National Institute of Mental Health (Protocol LSN-11). Three adult nonhuman primates (*Macaca mulatta*; 1 male, 2 females; 7–8 years old) received two chronic implantations of high-density 96-microelectrode arrays (Blackrock Microsystems; 4×4 mm^2; 400 µm interelectrode distance; 10×10 grid with corner grounds). To direct recordings towards superficial cortical layer II/III, electrode shanks of 0.6 mm length were used in prefrontal cortex (PFC; $n = 4$), and shanks of 1 mm length where used for premotor cortex (PM; $n = 2$). During recording sessions monkeys sat head-fixed and alert in a monkey chair with no behavioral task given. Portions of this dataset have been analyzed previously (2, 60).

3.2.2 Electrophysiological recordings and preprocessing

Simultaneous and continuous extracellular recordings were obtained for 12 – 60 min per recording session (2 kHz sampling frequency), filtered between 1 – 100 Hz (6th-order Butterworth filter) to obtain the LFP, and notch-filtered (60 Hz) to reduce line noise. About 7 ± 3% of time periods were removed from functional electrodes due to artifacts introduced by e.g. vocalization, chewing, sudden movements. These artifacts were identified by threshold crossing (SD > 7) and excised (± 0.25 s). Arrays on average contained 85 ± 8 functional electrodes that exhibited 64 ± 50 µV of spontaneous LFP fluctuations (SD). Electrode LFPs were z-transformed and recording sessions for each array were combined for further analysis. The current study represents a combined 22 hr of ongoing cortical LFP activity (Table 3.1).

	Recording Time (min)	Recording Sessions (n)	Recording Span (*wks*)	Functioning Electrodes (n)	Artifact Removal (%)	SD (μV)
V-PF	167	6	2	91	2.5	25
V-PM	208	7	2	91	5.3	35
N-PF	135	7	8	89	9.9	35
N-PM	122	4	6	71	6.0	35
K-PF1	562	19	11	81	7.0	140
K-PF2	118	4	1	91	9.2	115
avg ± STD	219 ± 171	6 ± 6	8 ± 4	85 ± 8	7 ± 3	64 ± 50

Table 3.1: Summary of nonhuman primate LFP recordings analyzed in the current study. *Recording Time*: Total duration of recordings concatenated over multiple recording sessions separated by up to several days. *Recording Sessions*: Number of resting-state recording sessions. *Recording Span*: Number of weeks over which the session data were collected. *Working Electrodes*: Number of electrodes showing adequate signal-to-noise ratio (<~7SD) out of 96 electrodes on the array. *Cleaning reduction*: Percentage of recording time removed due to artifacts caused by i.e. vocalization, sudden movements, chewing, etc. *SD*: Standard deviation of post-cleaning channel activity, averaged over all working electrodes. *X*: Monkey *PM*: Premotor cortex. *PF*: Prefrontal cortex. Monkey K had two arrays in PF, whereas monkeys N & V had 1 array in PM and PF each.

3.2.3 Power spectrum analysis

Single electrode periodograms (Mathworks; *pwelch*) were averaged for each array and displayed in double-logarithmic coordinates. Intensity of prominent γ-oscillation was obtained for each electrode by subtracting a power-matched 1/*f* fit from the original periodogram and dividing the area under the resulting curve from $\omega_{peak} \pm 1$ Hz by the integral over the range $\omega_{peak} \pm 5$ Hz. We note that 25 – 35 Hz oscillations are at the lower region of the γ–band (93) and have also been identified as the β_2 sub-band in nonhuman primate PF and PM (13).

3.2.4 Avalanche definition

For each electrode in the array, absolute peak amplitude and time of negative LFP threshold crossings (–2 SD) were extracted at $\Delta t = 0.5$ ms and combined into a matrix, i.e. raster, with rows representing electrodes and columns representing time steps. Binary rasters were created by setting amplitude values to 1. Rasters at reduced temporal resolutions were obtained by concatenating columns and summing amplitude values. Based on a population time vector, obtained by summing nLFPs in the raster for each time step, avalanches were defined as spatiotemporal continuous activity in the population vector bracketed by at least one time bin of no activity. The size of an avalanche, *S*, was defined as the number of nLFPs participating. Multiple nLFPs at an electrode during an avalanche are rare (2) and were counted in size estimates. Avalanche lifetime, L, was defined as the number of successive time bins spanned by an avalanche in multiples of temporal resolution Δt. Avalanche duration, *T*, was expressed in absolute time as $T = L * \Delta t$. Scale invariance of *S*, *L* or *T* was visualized by plotting probability distributions *P(S), P(L),* and *P(T)* in log-log coordinates. For some analyses, Δt was set to the average inter-event interval (<IEI>) which was unique for each array (Table 3.2); for other analyses, Δt was explored as a parameter between 1 – 30 ms in 0.5 ms increments.

	⟨IEI⟩ (ms)	Event Rate (Hz)	$\langle IEI \rangle_{1\text{-}20\ Hz}$ (ms)
V-PF	2.42	4.61	9.97
V-PM	3.60	3.02	16.00
N-PF	4.00	2.59	16.42
N-PM	3.90	3.55	16.28
K-PF1	3.52	2.96	13.32
K-PF2	2.88	3.75	11.61
avg ± STD	3.39 ± 0.62	3.37 ± 0.34	13.9 ± 2.7

Table 3.2: Average nLFP event statistics on the array were similar across NHP and cortical area examined. LFP thresholded at -2SD. *Average Inter-Event Interval (<IEI>):* Average duration of silence between successive suprathreshold (< -2SD) nLFP events on the array binned at sampling frequency (2 kHz). *Event Rate*: Frequency at which suprathreshold nLFP events were detected. For legend see also Table 3.1.

3.2.5 Statistical tests and slope estimates

Maximum log-likelihood ratios (LLR) were calculated to test potential power law distributions against the alternatives of exponential distributions if not stated otherwise (16). As a control, we also tested against log-normal distributions. Significance of the LLR was determined according to previously published methods (16, 94) and confirmed LLR results.

Estimations of initial slope were based on linear regression of log-converted data excluding higher cut-off effects. For α, we used the range of $S = 1$ to 40, which excludes the distribution cut-off close to the total number of functional electrodes on the array ($n \geq 70$). Initial slopes β of $P(L)$ and χ of $\langle S \rangle(L)$ were estimated from $L = 1\Delta t$ to $5\Delta t$.

3.2.6 Collapse of the temporal profile of avalanches

Avalanches were grouped by L in multiples of Δt and averaged to obtain the average temporal profile for a given lifetime, $\langle S\rangle(t, L)$.

$$\langle S\rangle(t, L) \sim L^{\chi-1}\ \mathcal{F}\left(\frac{t}{L}\right) \tag{3.1}$$

The shape collapse function, shown in Equation 3.1, relates the mean profile for each lifetime L, $\langle S\rangle(t, L)$, with a characteristic temporal profile $\boldsymbol{\mathcal{F}}(t/L)$, and scaling factor, $L^{\chi-1}$, that is independent of L. Normalized to fractional time unit t/L, amplitudes were then rescaled via Equation 3.1. To perform a local shape collapse, we plotted $\langle S\rangle(t, L)$ from L-1 through L+1 for L_{min} = 3Δt (to reduce finite size effects in shape caused by too few data points) through $L = L_{max}$ chosen based on the strength of our data set (>1,000 avalanches per L). The error of the collapse, Δ_F, was quantified via a normalized mean squared error (NMSE) of height-normalized individual profiles to the combined normalized average of all collapsed profiles. Minimized collapse error was calculated by scanning through χ = 0.5 to 3 at resolution of 0.001 to find the collapse in avalanche waveform associated with the smallest Δ_F via χ_{collapse}. An $\Delta_F > 1$ was considered a failure in collapse.

3.2.7 Parabolic fit

For the parabolic fit we used the approach by Laurson (85) as follows:

$$y = A * \frac{t}{T}\left(1 - \frac{t}{T}\right)^{\gamma-0.5} \tag{3.2}$$

The parabolic fit error, Δ_F, was quantified via a normalized mean squared error (NMSE) of individual profiles to an amplitude-matched parabola which was coarsegrained to match L. Comparison to a semicircle fit was conducted in the same manner, with the following substitution:

$$y = A * \sqrt{1 - \left({}^{t}/_{T}\right)^{2}} \tag{3.3}$$

3.2.8 LFP waveforms

To trace the oscillation origin of deviations from the parabolic shape motif, neuronal avalanche temporal profiles were compared to their corresponding LFP waveforms with sampling frequency 2 kHz. Waveforms were grouped by L and averaged. Single electrode averages were used to calculate the array average.

3.3 Results

3.3.1 Neuronal avalanches and oscillations co-exist in ongoing brain activity

In order to study the temporal profile of neuronal avalanches, we must first address dominant dynamics that shape the temporal organization of brain activity. To this end, we study the cortex of nonhuman primates and demonstrate that neuronal avalanches co-exist with oscillations in the ongoing local field potential (LFP). Using chronically implanted high-density microelectrode arrays, the ongoing LFP (1 – 100 Hz) was recorded in premotor (PM, $n = 2$) and prefrontal cortex (PF, $n = 4$) of three nonhuman primates (*Macaca mulatta*; K, V, N) sitting in a monkey chair. The animals were awake during the recording sessions but were not engaged in behavioral tasks. About 4 ± 2 hr of activity were analyzed during 9 ± 7 recording sessions over the course of 5 ± 4 weeks (85 ± 8 electrodes/array; Table 3.1).

Avalanches were identified first by extracting, for each electrode, negative LFP transients (nLFPs) exceeding a threshold of -2 standard deviations (Fig. 3.1*A*). nLFPs occurred at a rate of 3.4 ± 0.3 Hz per electrode and were separated on the array by an average inter-event interval $\langle \mathrm{IEI} \rangle = 3.4 \pm 0.6$ ms (Table 3.2; $n = 6$ arrays). In line with experiments (5, 55) and theory (32), we then concatenated successive time bins with nLFPs on the array at temporal resolution $\Delta t = \langle \mathrm{IEI} \rangle$ into nLFP clusters (Fig. 3.1*B*). We found that nLFP cluster size, S, i.e. the number of nLFPs in each cluster, distributed as a power law with a slope $\alpha \cong 3/2$, the hallmark of neuronal avalanches (Fig. 3.1*C*; power law vs. exponential $\mathrm{LLR} \gg 10^4$, $p < 0.001$). In contrast, the duration distribution of avalanches did not follow a power law and no duration slope β could be obtained at $\Delta t = \langle \mathrm{IEI} \rangle$ ($\mathrm{LLR} < 0$; $p > 0.1$ (94) Fig. 3.1*D*). Instead, durations T, or, alternatively, lifetimes $L = T/\Delta t$, distributed shorter than expected and were closer to an exponential distribution. This suggested the presence of a secondary process affecting avalanche durations. Indeed, the average periodogram of the continuous LFP, besides having a $1/f^a$ decay with $a \cong 1$ (95), indicated a prominent oscillation in the low γ-regime at 29.3 ± 1.7 Hz (92, 93) ($n = 6$ arrays; Fig. 3.1*E*). These oscillations, which we will refer to simply as γ-activity, were variable in peak frequency and intensity, spatially heterogeneous and differed significantly between arrays and areas (Fig. 3.1*F*; $p < 0.001$, ANOVA, $F_{\mathrm{int}} = 133.6$, $F_{\mathrm{freq}} = 86.1$).

Theory (35, 84-86) predicts that the quotient of size and duration slopes, $(\beta-1)/(\alpha-1)$, provides the scaling exponent of avalanche profiles, χ. Yet, our initial results show that the slope β does not exist at the temporal resolution given by event occurrences. We hypothesize that the deviation of the lifetime distribution from a power law is related

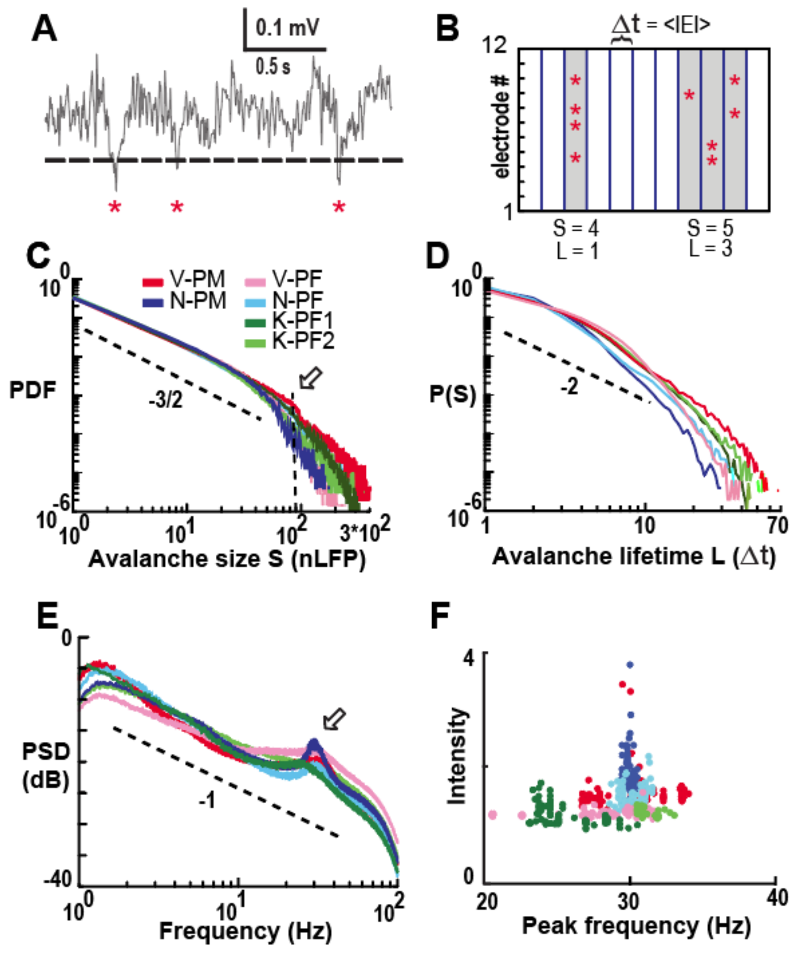

Figure 3.1: Neuronal avalanches and γ–oscillations co-exist during cortical resting activity of nonhuman primates. ***A***, Ongoing single electrode LFP with negative threshold crossing (2SD; broken line) defines nLFP times and peaks (*asterisks*). ***B***, Concatenating successive time bins with at least 1 nLFP defines nLFP clusters of size 4, 5 (*gray*) at temporal resolution Δt on a 12-electrode array (*schematics*). **C**, Power law in nLFP cluster sizes identifies avalanche dynamics ($\Delta t = \langle \mathrm{IEI} \rangle$). *Broken line*: power law with slope -3/2. *Arrow*: cut-off at ~90 electrodes (2). ***D***, Non-power law duration distributions of nLFP clusters at $\Delta t = \langle \mathrm{IEI} \rangle$. ***E***, Power spectrum density (PSD) of the LFP with γ–activity peaks at 25 – 35 Hz. Average PSD per array (*color coded*) from single electrode PSDs. *Broken line*: 1/*f*. ***F***, Peak frequency vs.1/*f*-corrected γ–intensity for each electrode. Legend in *C* applies to *D* – *F*.

to the presence of γ -activity. Accordingly, we set out to identify temporal regimes for which both size and duration distributions of avalanches exhibit valid slopes and the influence of γ -activity is minimized.

3.3.2 γ-activity affects avalanche duration and size-duration relationship

To identify potential temporal domains that minimize interference of γ-oscillations with avalanche parameter estimates, we systematically assessed avalanche parameters for temporal resolutions $\Delta t = 1 - 30$ ms in steps of 0.5 ms. Previous work has shown that an increase in Δt retains the power law in avalanche size while systematically reducing the corresponding slope α (2, 5, 55, 96, 97). Here we extended this approach to avalanche duration in monkey. Indeed, distributions for size and duration systematically changed with increase in Δt (Figs. 3.2*A, B*). Power laws were maintained for size (Fig. 3.2*C*; LLR $>> 10^3$; vs. exponential; $p << 0.005$), with a steady shift in the cut-off and decrease in α (Fig. 3.2*E*). Importantly, whereas duration distributions failed the power law test for intermediate Δt as shown above (Figs. 3.2*D&F*, *gray area*), they exhibited distinct power laws at high and low temporal resolution (LLR $>> 10^3$; vs. exponential; $p < 0.005$). Similar results were obtained when testing against log-normal alternative distributions (Fig. 3.3).

Theory and experiment link the average size of avalanches with given duration T, $\langle S\rangle(T)$, to the avalanche profile (35, 86). More specifically, the slope of $\langle S\rangle(T)$, χ_{slope}, provides the scaling exponent for the collapse of avalanche profiles (Fig. 3.2*G*). This estimated slope was closer to a value of 2 for valid power law duration regimes,

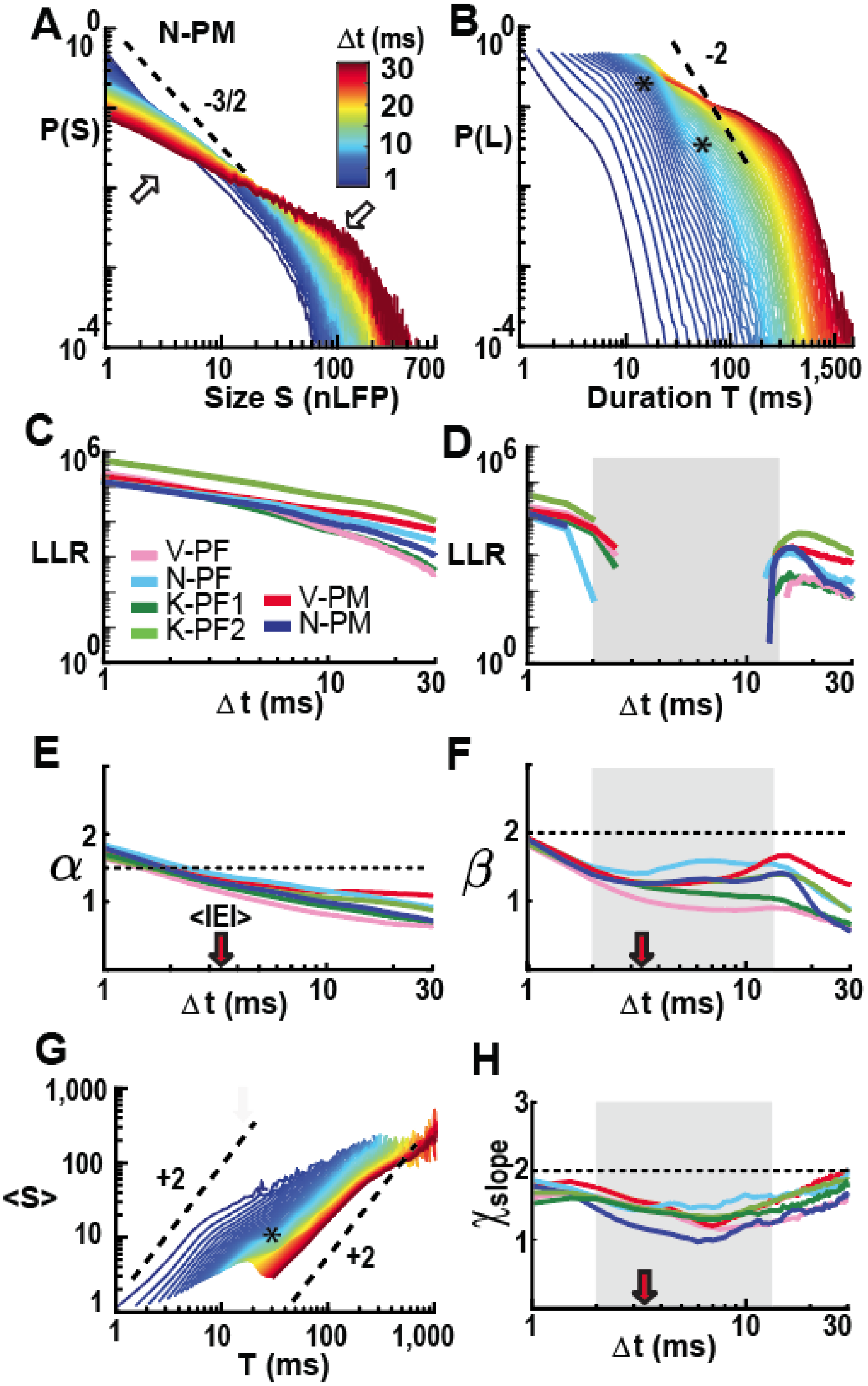

Figure 3.2: Systematic variation of temporal resolution identifies avalanche profile regimes with estimated scaling exponent close to 2. *A*, Size distributions (single nonhuman

primate; N-PM) decrease in slope (*upward arrow*) with increase in Δt and corresponding rightward shift in cut-off (*downward arrow*). ***B***, Corresponding dependence of duration distribution on Δt. Note deformations (*asterisks*) at intermediate Δt. ***C***, Size distributions remain power laws for all Δt (LLR values > 0 significant; vs. exponential distribution; all arrays; *color coded*). ***D***, Corresponding summary for duration distributions, which lose power law form at intermediate Δt (LLR < 0; *grey area;* all arrays). ***E***, Summary of decrease in slope α as a function of Δt. ***F***, Summary of slope β, which plateaus at intermediate Δt (*grey area taken from* D). ***G***, Mean-size per duration, ⟨S⟩(T), reveals deformations (*asterisks*) at intermediate Δt. ***H***, χ_{slope} estimates are depressed at intermediate Δt. *Red arrows*: <IEI> for all arrays. *Broken lines*: power law with given slope as visual guide.

whereas it approached 1 – 1.5 for intermediate Δt (Fig. 3.2*H*). These results demonstrate that the estimate of power law exponents and corresponding scaling relationships clearly depend on the temporal resolution of the analysis.

As further controls, we estimated χ_{slope} for Δt = 30 – 100 ms in the 3 arrays that provided sufficient number of avalanches at such coarse resolution. As shown in Fig. 3.4, the size and duration distribution cut-offs were clearly identifiable by a transition to a scaling exponent of $\chi_{\text{slope}} = 1$. This transition from the power law regime to the distribution cut-off demonstrates that uncorrelated activity in our data shifts to size-duration relationships for which cluster size simply grows linearly with cluster duration.

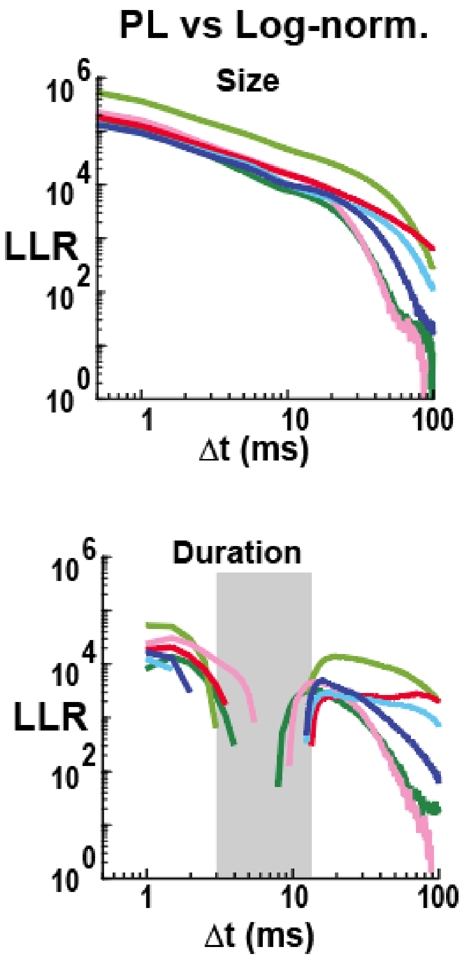

Figure 3.3: Log-likelihood test of neuronal avalanche size and duration distributions for 1–100 Hz LFP. **A,** Log-likelihood ratio comparing power law vs. log-normal distribution fits to the distributions of avalanche size (*top*) and avalanche duration (*bottom*) for decreasing temporal resolution and all arrays (for color code see Fig. 3.1). Note LLR of avalanche lifetime distributions reveals a range of Δt from 3–15 ms, for which most durations deviate from a power law (LLR < 0; $p > 0.1$) and where the power law slope β is accordingly ill-defined (*grey area*).

3.3.3 The scale-invariant, inverted parabolic temporal profile of avalanches

To further demonstrate the impact of γ-activity on profile estimates, we directly calculated avalanche profiles for different Δt. Critical theory predicts the avalanche profile to be an inverted parabola independent of duration T (35, 86, 98). As seen in Figure 3.5*A*, avalanche profiles largely follow an inverted-parabola at high and low Δt. However, the profile deviated from a parabola at intermediate Δt for which profiles track multiple γ–cycles on the array (Fig. 3.5*A*; middle). Accordingly, when analyzing

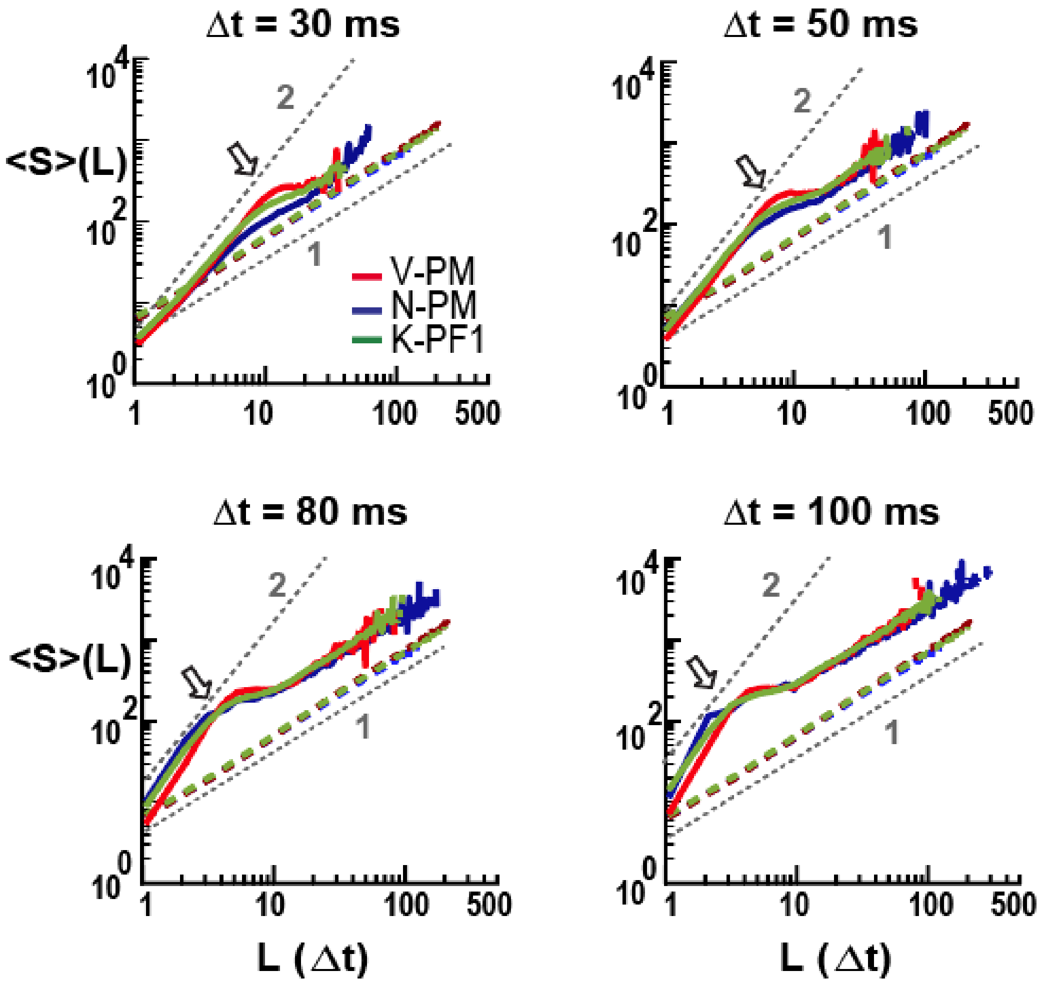

Figure 3.4: Shift in ⟨S⟩(L) power law-cutoff shows creeping transition from critical to linear trend for overly coarse temporal resolutions. Mean size-per-lifetime, ⟨S⟩(L), at time resolutions Δt = 30, 50, 80, 100 ms in a subset of subjects (*top left* through *bottom right*, *color coded*). *Black dotted lines*: Visual guides of given power law slopes. *Arrows*: Elbows in ⟨S⟩(L) are associated with the transition to P(S) and P(L) power law cutoffs, where cluster size simply grows linearly with cluster duration.

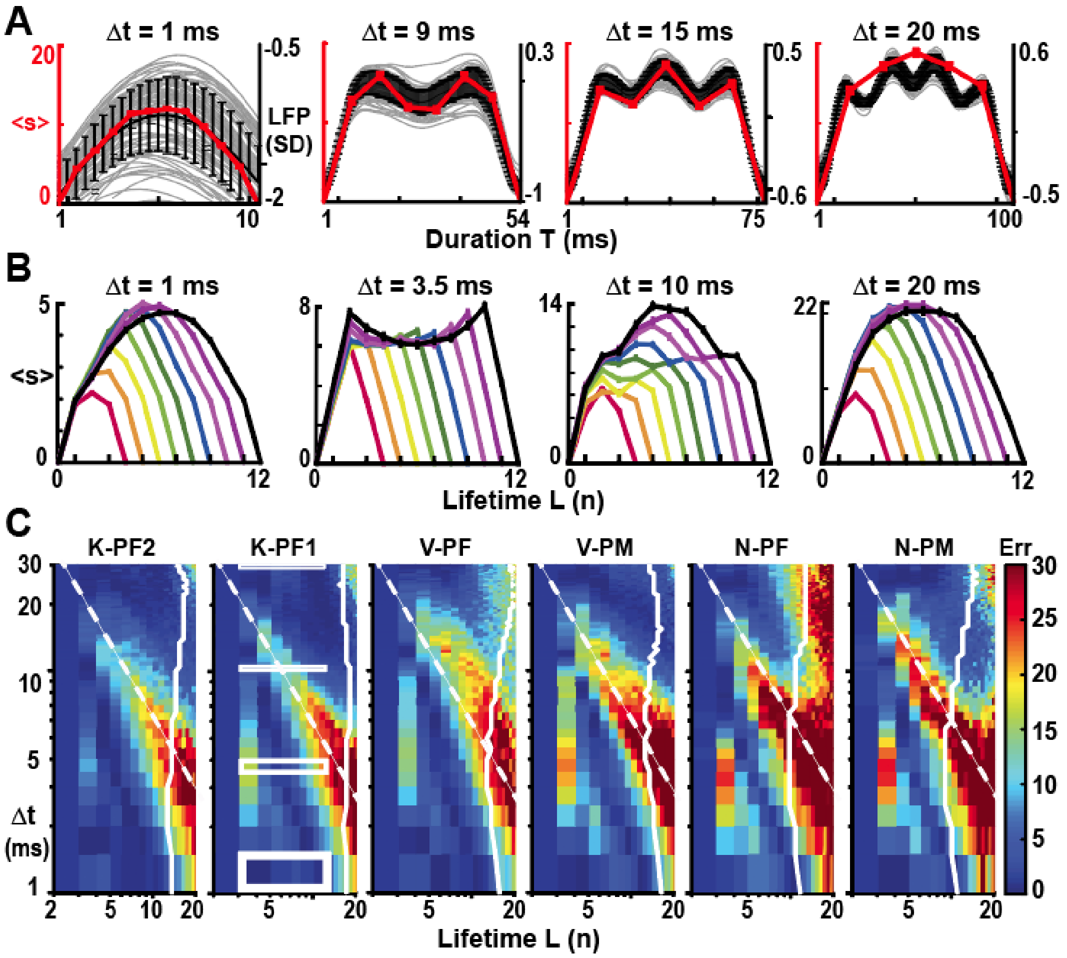

Figure 3.5: The inverted parabolic profile of neuronal avalanches is modulated by γ–activity at intermediate Δt. ***A*****,** Examples of temporal avalanche profiles (*red*: mean size-per-timestep ± se; N-PM) at increasing Δt and corresponding underlying γ–oscillations in the LFP (*Grey*: inverted LFP of single electrode; *black*: mean ± sd of the array). ***B***, Variable profiles are bracketed by parabolic shapes at low and high Δt for lifetimes L = 3, …, 11 (mean ± se; K-PF1). ***C***, Density plot of fit quality to an inverted parabola for all arrays and all profiles in the (L, Δt)– plane. Note compact regions of high deviations from a parabola surrounded by good parabolic fits. Rectangular regions in K-PF1 indicate profile ranges displayed in *B*. *Broken lines*: High Δ_F for condition T = L * Δt ≅ 66 ms.

avalanches grouped by lifetime L, we find scale-invariant profiles at high and low, but not intermediate Δt (Fig. 3.5*B*). We quantified this relationship for all 6 arrays in corresponding error density plots in the (L, Δt)-plane. Strongest systematic deviations from a parabola were uncovered for $T = L * \Delta t \cong 66$ ms which spans ~2 γ-cycles at 30 Hz (Fig. 3.5*C*; *broken lines*).

The demonstration of regimes with good parabolic fits paved the way for identifying a scale-invariant temporal profile $\mathcal{F}(t/L)$ over a range of L (M & M; Equation 3.1). According to theory, $\mathcal{F}(t/L)$ can be obtained by scaling $\langle S_L \rangle$ with $L^{\chi-1}$, collapsing each profile. We therefore estimated $\mathcal{F}(t/L)$ directly by finding χ_{collapse}, the estimate of χ that provided us with the lowest collapse error, Δ_F, over an extended range of L and different Δt (Fig. 3.6). Example profiles for $L = 3$ to 11, their corresponding best collapse, χ_{collapse}, as well as residual profile differences together demonstrate good collapse with χ_{collapse} close to 2 at high and low, but not intermediate Δt (Fig. 3.6*A*-*C*). To further delineate the impact of γ-activity on profile collapse, we systematically identified non-collapsible regions in the (L, Δt)–plane by plotting Δ_F for the local collapse of (L–1, L, L+1) as a function of Δt (Fig. 3.6*D*). This collapse approach revealed a band of high Δ_F for $T = L \times \Delta t \cong 40$ ms for all arrays, located at the transition from 1- to 2-peaked profiles. We note that the high Δ_F band was solidly placed within the power law regime (*broken line*) and thus, does not indicate weak statistics due to e.g. a low number of avalanches as found beyond the cut-off regime (*cf.* Figs. 3.1, 3.2). The average collapse error, $\langle \Delta_F \rangle$, significantly correlated with γ-intensity across arrays, confirming that the band of high Δ_F reflects γ-activity (Fig. 3.6*E*; $p = 0.0054$). χ_{collapse} was close to 2 for temporal resolutions least affected by γ-activity (Fig. 3.6*F*) and the collapsed profile

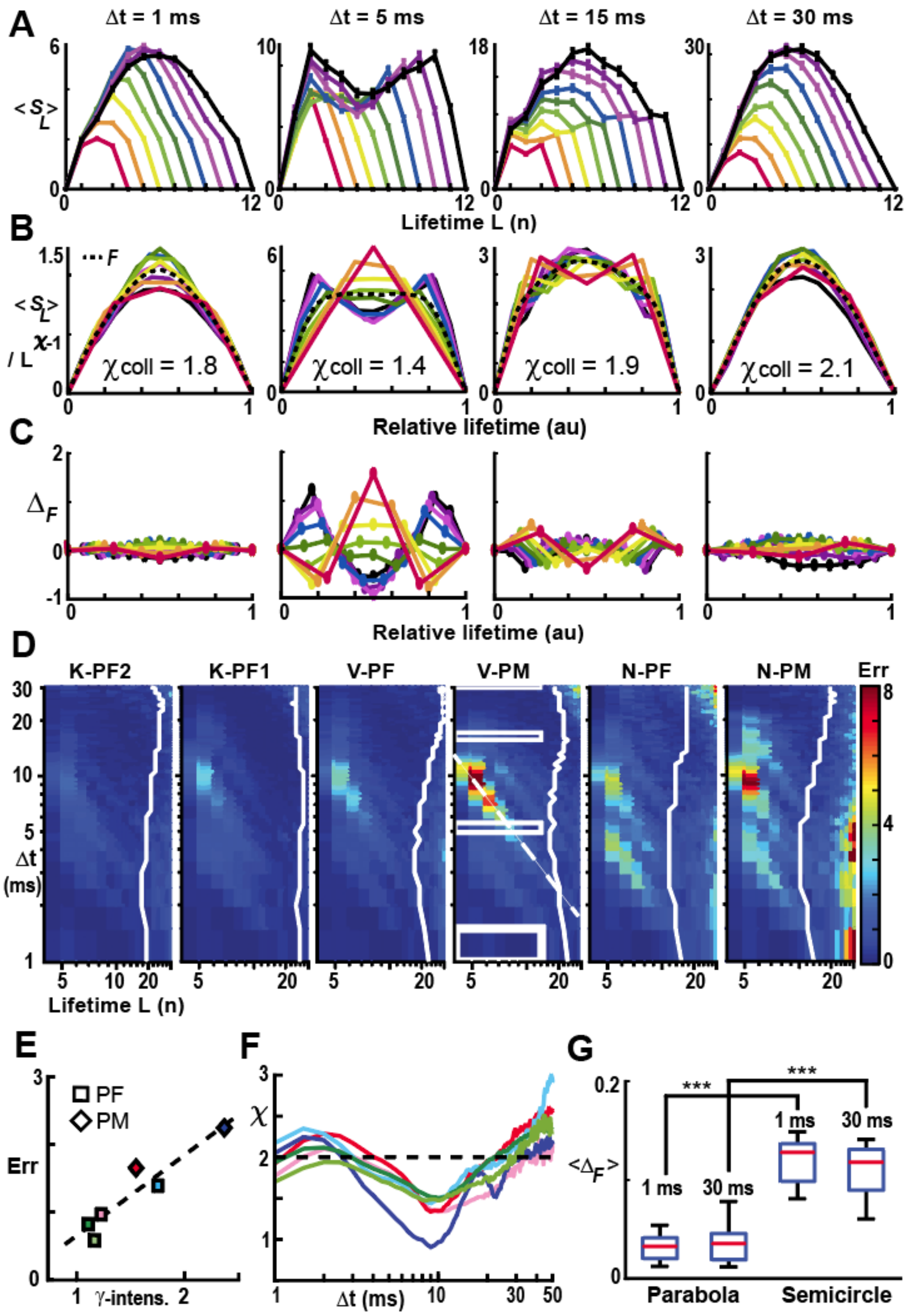

Figure 3.6: Scaling collapse of the inverted parabolic profile of neuronal avalanches. ***A***, Examples of the average temporal profile $\langle S_L \rangle(n)$ for avalanches of lifetime L = 3, …, 11 (*color coded*; mean ± se) at temporal resolution Δt = 1, 5, 15 and 30 ms (single nonhuman primate; V-PM). ***B***, Corresponding profile collapse with duration normalized by L and $\langle S_L \rangle(n)$ scaled

by $L^{\chi-1}$. $\chi_{collapse}$ (χ_{coll}) obtained from best parabolic collapse $\boldsymbol{\mathcal{F}}(t/L)$ (*dotted line*; see Material and Methods). **C**, Profile collapse differences, Δ_F, obtained by subtracting best collapse $\boldsymbol{\mathcal{F}}(t/L)$ from normalized profiles, are largely symmetrical around profile peak. ***D***, Density plot of collapse error for all 6 arrays ranked from low (*left*) to high γ–oscillation power (*right*). Collapse error obtained from profiles L_{-1}, L, and L_{+1} for given Δt. Collapse failure visible for intermediate Δt before the cut-off in lifetime distribution (*white border* equals threshold for L with <1000 avalanches indicating statistical cut-off regime). ***E***, Average collapse error positively correlates with γ–intensity across arrays ($p = 0.005$; *color code c.f.* Fig. 3.1*A*). ***F***, Summary of χ_{coll} obtained as a function of Δt (Temporal profile collapse $L_{3\text{-}5}$). χ_{coll} is close to 2 outside γ–activity impact. ***G***, A parabola consistently fits the temporal avalanche profile better than a semicircle. Error bars represent array mean ± sd.

was significantly closer to a parabola than to a semicircle (Fig. 3.6*G*; ANOVA; $p = 1.4 * 10^{-6}$; F = 22.2), the latter being predicted for non-critical dynamics.

If γ-activity is simply linearly superimposed on an otherwise scale-invariant avalanche background, bandpass filtering between 1 – 20 Hz which reduces γ-activity should not effect estimates of avalanche parameters. Bandpass filtering reduced the rate of nLFPs, yet a sufficient number of avalanches were obtained in $n = 3$ arrays (⟨IEI⟩ = 15.2 ± 1.6 ms; $n = 3$; Fig. 3.7). To account for the longer ⟨IEI⟩, we extended our analysis for Δt up to 100 ms. Power laws for size distributions were maintained for all temporal resolutions (LLR >> 10^3; $p < 0.005$). However, duration distributions now failed the power law test for a new range of Δt = 8 – 25 ms, which is closer to the scale of β-oscillations (Fig. 3.7*B, red arrow and grey shading*). Similarly, profile collapses

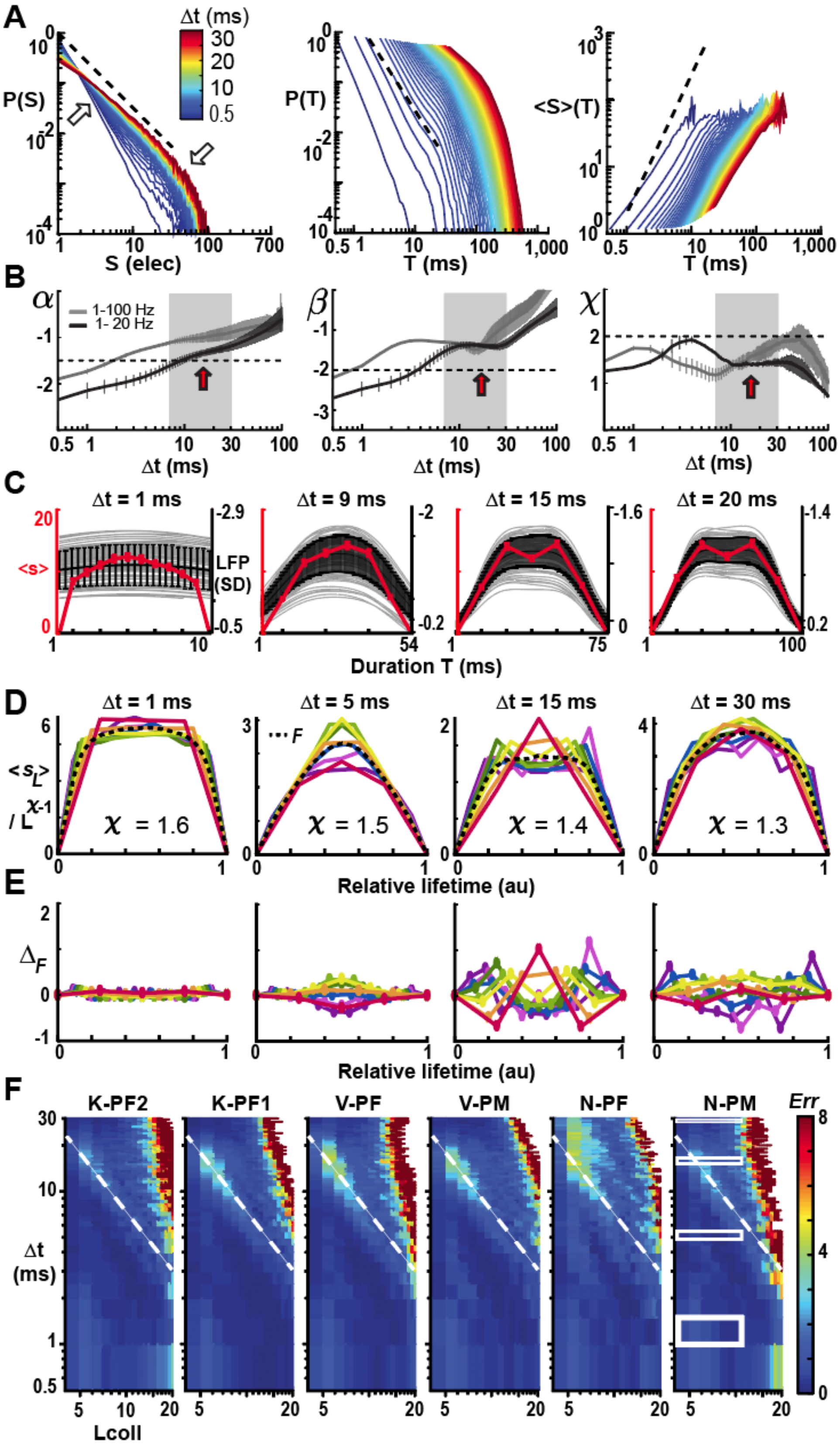
A
Δt (ms)
30
20
10
0.5
P(S)
S (elec)
P(T)
T (ms)
<S>(T)
B
α
1-100 Hz
1- 20 Hz
β
χ
Δt (ms)
C
Δt = 1 ms
Δt = 9 ms
Δt = 15 ms
Δt = 20 ms
<s>
LFP (SD)
Duration T (ms)
D
Δt = 1 ms
Δt = 5 ms
Δt = 15 ms
Δt = 30 ms
$<s_L> / L^{\chi-1}$
F
χ = 1.6
χ = 1.5
χ = 1.4
χ = 1.3
Relative lifetime (au)
E
Δ_F
Relative lifetime (au)
F
K-PF2
K-PF1
V-PF
V-PM
N-PF
N-PM
Err
Δt (ms)
Lcoll

Figure 3.7: Reduction of γ–activity recovers power laws, scaling exponent, and parabolic profile at the scale of γ–oscillations, and shifts analogous influences on avalanche dynamics to β–activity. A, Avalanche size distributions, durations, and mean-size-per-duration ⟨S⟩(T) as a function of Δt for data bandpass filtered between 1–20 Hz (Butterworth 6th order). Note presence of approximate power law in P(S), P(T) and ⟨S⟩(T) plot (*cf.* Fig. 1D). **B,** Smooth increase in size distribution slope, α, with increasing Δt up to 100 ms (*left*), but variable slope changes for duration distributions (*middle*) and ⟨S⟩(T) (*right*) at intermediate Δt are shifted to the right towards β–oscillations when **γ** power is reduced (*red*) (*cf.* Fig. 3.1*E*). *Grey*: 1–100 Hz mean ± sd; average over 3 monkeys. *Black*: 1–20 Hz mean ± sd. *Red arrows:* ⟨IEI⟩ for 1-20 Hz. *Black broken lines*: Visual guides of theoretical power law slopes. **C**, Examples of continuous LFP waveforms. **D**, After removal of γ–oscillations, temporal profiles can be collapsed over a wide range of temporal resolutions Δt (*cf.* Fig. 3.3) revealing a new domain of reduced collapse which traces slower β–oscillations. **E,** Symmetrical difference of normalized profiles from best parabolic fit. **F,** Density plot of collapse error obtained from profiles L_{-1}, L, and L_{+1} for given Δt. Region of collapse failure starts at large Δt before the cut-off in lifetime distributions. *Broken lines*: High collapse error Δ_F for condition T = Lx Δt ≈ 100 ms. Rectangular regions in N-PM indicate profile ranges displayed in A, C, D, and E.

previously affected at the scale of γ-activity improved (Fig. 3.7*D*, *middle-left*), while double-peaked profiles shifted to lower resolutions with profile collapse strongly affected for $T = L * \Delta t \cong 75$ ms (*broken line*) equivalent to the transition from one to two β–cycles at 20 Hz (Fig. 3.7*C–F*). Importantly, profile collapse now consistently revealed $\chi_{\text{collapse}} < 1.5$ suggesting γ-activity to be an essential element for a critical scaling exponent χ_{collapse} close to 2. These findings suggest that γ-activity does not simply arise from a secondary process superimposed onto neuronal avalanches, but instead is an inherent dynamical phenotype embedded in critical brain dynamics.

3.4 Discussion

The present work uncovers a scale-invariant temporal parabola in the organization of ongoing neuronal avalanches, a finding in line with expectation for critical dynamics. Previous work in *in vitro* preparations and in rodents reported nested θ/β/γ-oscillations (12, 34) embedded in avalanches. Simulations also suggested oscillations can emerge during avalanches (46, 47, 99, 100). However, it had yet to be determined whether cortical avalanches in the awake mammal exhibit a distinct temporal profile that is scale-invariant, nor had it been known how that profile might relate to the scale of an oscillation. Here we demonstrated the motif of an inverted parabola that guides the scale-invariant temporal evolution of neuronal avalanches in the propagation of ongoing cortical activity *in vivo*. This motif uncovers a specific constraint for ongoing cortical dynamics, that is, local events initiate spatial expansion that i) is similar at all scales and ii) collapses symmetrical in time. Thus, despite the temporal evolution of activity within an avalanche, the profile exhibits time reversal (85).

This motif and its corresponding collapse is predicted by theory of critical systems (35, 84-86, 98) which also states that the exponents of the power law distribution in size, α, and duration, β, relate to the collapse exponent as $\frac{\beta-1}{\alpha-1} = \chi$ (35). For neuronal avalanches, empirical (5) and simulated (33) slopes of α are close to an exponent of 3/2 at $\Delta t = \langle \mathrm{IEI} \rangle$. These empirical insights have been recently confirmed within the Landau-Ginzburg theoretical framework of network dynamics (32). The size exponent of 3/2 is also characteristic for a critical branching process in line with the well-established empirical finding of a critical branching parameter of 1 for neuronal avalanches (5). These insights would suggest a duration exponent $\beta = 2$ for avalanches with corresponding $\chi = 2$, however, empirically obtained lifetime distributions have been difficult to analyze due to their typically narrow range in values. Our analysis identifies a new element affecting lifetime distributions by showing that β cannot be reliably determined at $\langle \text{IEI} \rangle$ in the presence of γ-oscillations, leading to a corresponding depression in χ. Importantly χ comes close to the value of 2 as expected for avalanche dynamics when the impact of the oscillation is reduced as is found at temporal resolutions too fine or too coarse to resolve multiple cycles.

Scaling collapse of avalanche profiles has been suggested as an alternative to confirm avalanche dynamics instead of relying on power laws solely (87). While profiles utilize more information about avalanches than size or lifetime distributions, robust profile collapse covering long lifetimes requires corresponding orders of magnitude more data compared to distribution estimates. Our current analysis was based on ~3 million nLFP events per monkey with a corresponding high number of avalanches, which allowed us to reconstruct robust profiles even for long lifetimes, which are rare ($>7\times\Delta t$; *cf.* Fig. 3.2). This in turn enabled us to identify temporal resolutions of the parabolic motif with high collapse quality and to distinguish the modulating influence of γ–oscillations from profile variations due to reduced statistical power. We note that, by definition, avalanches start with the peak time of an nLFP, which synchronizes avalanches to the first oscillation peak on the array.

We demonstrate that, once γ–activity is removed, the variability in avalanche profile and corresponding changes in slope estimates shift to the scale of β–oscillations. This suggests that our approach might be valid to study the impact of even lower frequency oscillations on avalanche profiles, given that avalanches have been reported at much slower time scales in human fMRI (63). Scaling collapses have also been successfully employed to quantify the temporal organization of behavior (81).

Our identification of a symmetrical (in time), parabolic profile for neuronal avalanches *in vivo* supports results in simulations of critical neural networks (87, 96) and identifies constraints for other generative models proposed for avalanche dynamics (89). Models fine-tuned to produce power laws for size and duration distributions via bi-stable dynamics combined with a locally expansive dynamical term (91) or purely external uncorrelated driving (90) reveal profiles that deviate from a symmetric parabola. The parabolic profile also differentiates neuronal avalanches from stochastic processes with no memory which typically display a semicircle motif (101). Specific graph-theoretical constructs such as a hierarchical topology (52) can also mimic scale-free size distributions but fail to produce an inverted parabola profile. Network and biophysical models have demonstrated avalanches to emerge with oscillations at a particular E/I balance or topology; however, the corresponding avalanche profile was not reported (46, 102, 103). Our findings support a recent report by di Santo et al. (32) which demonstrates the emergence of avalanches at a continuous synchronization/desynchronization phase transition in co-existence with neuronal oscillations. Their mesoscopic model is a variation of network dynamics originally introduced by Cowan e.g. (100) but contains an expansive term. It exhibits critical exponents like those of a critical branching process, originally introduced to describe avalanche dynamics.

It is well accepted that limited predictability is one of the major disadvantages of critical systems. Functionally, our findings support recent suggestions (104) that the co-existence of temporal scales based on oscillations in the presence of critical dynamics might allow the brain to combine functional benefits of criticality for information processing (29, 56-60, 82, 83, 105) with the necessity of temporally precise behavioral outcome or learning rules that require a particular temporal scale such as spike timing dependent plasticity.

The precise profile of neuronal avalanches might be a suitable biomarker for pathological brain dynamics. In human preterm infants suffering from anoxia, asymmetric avalanche profiles in ongoing EEG activity became symmetrical upon recovery (30, 31), which is supported by our demonstration of a symmetric profile during normal activity. Conversely, γ–activity has been identified as a key marker in disease states such as schizophrenia (106). Our demonstration that γ–activity and avalanche profiles are non-trivially related supports the idea that mental disorders such as schizophrenia might indicate deviations from critical brain dynamics (20).

Chapter 4: Neuronal avalanches in a developmental mouse model for schizophrenia

This Chapter summarizes research in progress. S.R.M. collected the data with technical assistance from Samhita Sengupta.

This chapter presents work in progress towards detecting aberrant neuronal avalanche dynamics in a developmental mouse model for schizophrenia. In the preceding Chapters, we established that the healthy neural state in mammalian cortex is characterized by scale-invariant dynamics balanced between excitatory (glutamatergic) and inhibitory (GABAergic) contributions to collective spiking activity. The present study is motivated by a need to elucidate the role of specific cell types in maintaining healthy brain activity in awake and behaving mice, specifically identifying the contribution of PV, SST, and VIP inhibitory populations to synchrony among excitatory principle cells. Previous research has pointed to GABAergic signaling dysfunction as a cause of positive and negative symptoms in schizophrenia, however, the specific population-level manifestations of disturbed neuronal activity patterns are unknown. A recent study implementing perinatal exposure to the NMDA receptor antagonist phencyclidine (PCP) to elicit schizophrenia-like symptomatology in rats revealed altered neuronal avalanche organization in adolescent, lightly-anesthetized animals (20). Observing neural activity while manipulating inhibitory cell ensembles may advance scientific understanding of disorganization and deficits exhibited by awake, adult mice treated perinatally with PCP.

Using two-photon calcium imaging and optogenetics in PV-Cre, SST-Cre, and VIP-

Cre transgenic mouse lines, we anticipate that neuronal avalanche analysis can reveal precise, cell type-specific contributions to network dysfunction. To date, we have conducted behavioral assays of episodic memory in a total of 20 juvenile and adult mice and conducted 19 2-photon imaging sessions across 5 adult mice expressing the YC2.60 genetically-encoded calcium indicator (GECI). Our preliminary results in saline- and PCP-treated wild-type and PV-Cre mice establish signatures of neuronal avalanche activity in anterior cingulate cortex (ACC) in cortical layer II/III during free ambulation on a mouse wheel. Next steps in this study include rescuing behavioral and neural phenotypes with acute administration of the antipsychotic D-serine, which enhances NMDA receptor functioning thereby compensating for the developmental PCP-induced receptor dysfunction. Further, we will perform optogenetic manipulation of interneurons via virally-expressed channelrhodopsin (hCHR2, depolarizing) or halorhodopsin (eNpHR3.0, hyperpolarizing) in PV-, SST-, and VIP-Cre transgenic animals. Our specific aims are to determine whether neuronal avalanche analysis may 1) provide evidence in support of the validity of the perinatal PCP schizophrenia model, 2) reveal new insight into the structure of pathological network dynamics observed via microscopy, and 3) present diagnostic and prognostic capacity in the study and treatment of schizophrenia.

4.1 Introduction

For a person with schizophrenia, daily life may be marked by sensory and perceptual exaggerations of reality (positive symptoms) such as psychosis, paranoia, and auditory hallucinations. Even more debilitating (107) and difficult to treat (108) are negative symptoms including impaired memory, anhedonia, and depressed affect, which have been associated with reduced cortical thickness in brain areas responsible for cognitive function (109). Despite the cost to society and decades of research (3), the etiology of schizophrenia has evaded comprehensive characterization. While it is known that certain genetic factors contribute to schizophrenia risk (110, 111), much is left to be learned about the effect of insults to developing brain. Nor is it precisely known how current pharmacological treatments mechanistically reduce the severity of schizophrenia symptoms. With an overall prevalence of about 1% of the global population (112), identifying circuit alterations underlying cortical dysfunction and impaired cognition in schizophrenia is an urgent topic for the neuroscientific and psychiatric research communities.

To identify altered cortical dynamics, it is necessary to characterize the neurotypical state. Numerous findings suggest that the presence of critical brain dynamics indicates a healthy state of the brain (5, 22, 51, 55) at which gray matter functions are optimized (57, 59, 60). Pharmacological studies have shown that disrupting the excitation/inhibition (E/I) balance (28) or perturbing dopaminergic modulation of cortical circuits (113) can disrupt avalanche dynamics. It has also been shown that insults to cortical circuitry during vulnerable developmental periods can later result in ineffective or spurious cortical synchrony (114) and disorganized avalanche dynamics (20). Importantly, these distortions may underlie schizophrenic cognitive phenotypes.

NMDA hypofunction has been implicated in rodent pathophysiology and altered behavioral and anatomical phenotypes in adolescence and adulthood following neonatal exposure to NMDA receptor antagonists, with possible differential effects in male and female animals (115). The potent NMDA receptor (NMDAR) antagonist phencyclidine (PCP) is a commonly used agent for modeling schizophrenia in rodents, and a range of models are in current use. Acutely administered PCP is a typical model for psychosis, but this approach is limited by the confound of transient drug effects. An alternative method is subchronic drug administration: a 7-day course of PCP followed by a 7-day wash-out period. This allows residual drug and metabolites to leave the body and puts the animal into a withdrawal state analogous to mental illness. However, this approach lacks the developmental aspect central to the etiology of schizophrenia. A preferred method for approximating schizophrenia in rodents is prenatal or perinatal NMDAR antagonist exposure. The perinatal PCP model has been shown to produce a number of deficits including behavioral impairments, alterations in protein expression levels, and network dysfunction phenotypes that match trends seen in schizophrenia patients (116, 117). Another strength of the perinatal PCP disease model is that it is rescued by pharmacological treatments. Specifically, acutely administered D-serine (118) has been shown to rescue behavioral and neural phenotypes in rodents (20, 119). These studies on D-serine, an NMDA agonist with reduced serum levels in schizophrenia patients (118), present results supporting the hypothesis that increased excitatory activity may recruit GABAergic circuits to levels permitting healthy coordination of brain signals (120).

In addition to glutamatergic dysfunction, altered brain activity in schizophrenia has also been attributed to impairments in GABAergic signaling among interneurons (121, 122). This could contribute to two principle pathological conditions: hyperexcitability and disturbed network oscillations. Specific inhibitory cell types identified by marker genes parvalbumin (PV), somatostatin (SST), and vasoactive intestinal polypeptide

(VIP) may make unique contributions to episodic memory (123), and GABAergic cell populations may exhibit distinct alterations in schizophrenia (124, 125). For example, PV cell dysfunction is associated with a loss of precise temporal coding (126). This may underly the finding that PCP-treated animals demonstrated impaired episodic memory and excess cortical bursting (20). However, the potential contributions of SST and VIP cells to the behavioral deficits and altered cortical dynamics seen in schizophrenia are currently not well understood.

Here we present preliminary behavioral and cortical imaging results collected from male and female mice with perinatal exposure to PCP. Future steps include reversal of PCP-induced network alterations by treatment with established antipsychotics (e.g. D-serine) as well as optogenetic re-balancing of cortical circuits. These techniques may reveal insight into circuit-level mechanisms of pharmacological treatments, and further validate disrupted avalanche dynamics as a disease phenotype. Indeed, avalanches are regulated by some of the same pathways implicated in perinatal PCP cortical dysfunction, including the superficial layers of the anterior cingulate cortex (ACC) studied here. We specifically hypothesize that optogenetic excitation of PV and SST, but not VIP, cell ensembles will improve signatures of healthy brain activity in the adult brain following perinatal PCP exposure.

4.2 Methods

4.2.1 Transgenic mouse lines

All procedures were conducted in accordance with the NIH Animal Care and Use Committee (LSN-10). PV-Cre, SST-Cre, and VIP-Cre breeder pairs with a C57Blk6

	SAL	**PCP**	**Adol. NORT**	**Adult NORT**	**2PI**	**Adult NORT +D-serine**	**2PI + D-serine**	**2PI + opto**	**Total in study**
Total	8 (40)	11 (40)	19 (40)	19 (40)	5 (30)	(20)	(20)	(20)	19 (80)
Total Female	(20)	(20)	(20)	(20)	(15)	(10)	(10)	(10)	(40)
Total Male	(20)	(20)	(20)	(20)	(15)	(10)	(10)	(10)	(40)
WT Female	2 (5)	3 (5)	5 (10)	5 (10)	1 (8)	(5)	(5)	(5)	(10)
WT Male	3 (5)	3 (5)	6 (10)	6 (10)	2 (8)	(5)	(5)	(5)	(10)
PV-Cre Female	1 (5)	3 (5)	4 (10)	4 (10)	2 (8)	(5)	(5)	(5)	(10)
PV-Cre Male	2 (5)	2 (5)	4 (10)	4 (10)	1 (8)	(5)	(5)	(5)	(10)
SST-Cre Female	(5)	(5)	(10)	(10)	(8)	(5)	(5)	(5)	(10)
SST-Cre Male	(5)	(5)	(10)	(10)	(8)	(5)	(5)	(5)	(10)
VIP-Cre Female	(5)	(5)	(10)	(10)	(8)	(5)	(5)	(5)	(10)
VIP-Cre Male	(5)	(5)	(10)	(10)	(8)	(5)	(5)	(5)	(10)

Table 4.1: Animal group sizes. Experimental group size *N* across treatment group, sex, and transgenic strain. Planned group sizes are shown in parentheses.

background were purchased from Jackson Laboratory. Food and water were available *ad libitum* and animals were kept on a reverse light cycle (9pm - 9am). Mice were weaned at post-natal day P21 then co-housed and handled through adolescence (P25 –

P40). Animals were single-housed following cranial surgery (P42 - P180). See Figure 4.1*A* for a longitudinal experimental timeline.

Animal group sizes *N* as described in Table 4.1 according to developmental stage, sex, drug treatment group, and transgenic line. Planned group sizes are shown in parentheses. At the completion of this work, we expect to recruit sufficient cohorts to satisfy ~10 animals per group as shown in Table 4.1. Currently, animal group size N for behavioral data is as follows: SAL group, 20 mice; PCP group, 15 mice; WT/Cre$^-$ group, 24 mice; PV-Cre$^+$, 8 mice; SST-Cre$^+$, 4 mice; VIP-Cre+, 4 mice. Group sizes for calcium imaging are especially low due in part to low GECI expression. To date we have imaged 4 PCP-treated mice and 1 SAL-treated mouse.

4.2.2 Drug challenge

Littermates were numbered via ear notch on P7 and randomly assigned to PCP or SAL treatment groups with minor intervention to ensure approximately equal sex representation across groups. On P7, 9, and 11, phencyclidine (PCP, Cayman Chemicals) was dissolved in sterile saline to a concentration of 1 mg/mL, filtered (0.02 μm) under aseptic laminar airflow, and administered subcutaneously (10 μL/g aqueous PCP or pure saline) for a total dosage of 10 μg/g per day.

4.2.3 Surgery

Cranial windows for chronic imaging were installed as in (127). Briefly, mice of at least 7 weeks of age were anesthetized (isoflurane, 3% induction, 1-2% maintenance) on a Kopf surgical set-up and vital signs were monitored throughout surgery (MouseOx, Starr Systems). Animals were given subcutaneous anti-inflammatory steroid (dexamethasone, 0.2 mg/kg) one hour before surgery (128), antimuscarinic (Atropine, 0.2 mg/kg) and analgesic (Ketoprofen, 5 mg/kg) immediately preceding surgery, and antibiotic (Baytril, 0.23%) via drinking water for two weeks post-surgery. Following aseptic preparation of the surgical site, the skull was cleared via blunt dissection, a head bar was affixed with metabond (Parkell) over medial associative cortex, and a 3 mm diameter craniotomy was drilled over the anterior cingulate cortex (ACC). We then stereotaxically injected (34 G microinjection needle; Hamilton) 250 nL of virus (50 nL/min; 0.5:0.5 volume ratio when injecting multiple viruses) at 2-3 sites within ACC to target layer II/III (+1.5 mm AP, +0.5 mm ML, -0.15 mm DV). Glass windows (two stacked 3 mm windows bonded to a 5 mm base) were secured to the skull with non-reflective metabond for chronic imaging, and animals were allowed to recover for at least 7 days before further experimentation.

4.2.4 AAV virus

For 2-photon calcium imaging, we used the FRET-based Yellow Chameleon GECI (YC2.60, 10^13 viruses/mL, UNC Vector Core), which has a 1.5 s decay constant and effective cell localization for ROI registration and motion correction (22).

4.2.5 Novel object recognition test

Behavioral testing was conducted at the NIH Rodent Behavioral Core in a dedicated lab area with dimmable lights. The Novel Object Recognition Test (NORT) is an established assay of visual episodic memory (129) analogous to delayed matching-to-sample tests used in humans and primates (130). In rodents, NORT is a non-rewarded paradigm focused on spontaneous exploratory behavior. It is based on the principle that if mice are exposed to an object, subjected to a delay period, then presented with the same object as well as a novel object, they will recognize the original object and spend more time exploring the unfamiliar, novel object. If their episodic memory is impaired, they will not maintain a memory of the original object during the delay period and will subsequently treat both objects as novel. Rats treated with PCP have been shown to exhibit impaired novel object recognition (131).

Animals were habituated during adolescence to components of the behavioral experiment apparatus including the open behavioral box and paper transfer cups, as well as to the experimenters. Adolescent NOR testing took place between P25 and P40 and adult NOR testing took place between P60 and P120. For three days preceding NOR testing, mice were habituated for one hour each day to a testing box containing two metal platforms. Group-housed mice were habituated with cage-mates on the first day of habituation and individually on the second and third days. On the day of testing, animals were given an additional 3 minute habituation, followed by two 7 minute trials (acquisition and retention) separated by a 1 hour interval during which they were returned to the home cage. During the acquisition trial, two identical objects were placed on platforms in the arena (A1 and A2). During the retention trial, a third identical object and a novel object were placed in the arena (A3 and B). All phases including habituation, acquisition, and retention were recorded for up to 6 boxes simultaneously via a multiplexed feed for behavioral analysis. Object exploration was defined as sniffing, licking, or touching an object. Exploration time for each object were scored digitally using TopScan software (TopView Behavior Analyzing System, CLEVER Sys, Inc.).

In our NOR testing, Lego-based objects created in varying shapes and limited color pairs (red/yellow, blue/green, grey/black) with no natural significance (Fig. 4.1B, *upper*) were placed on standardized metal platforms (Fig. 4.1B, *lower*) to reliably position objects 8 cm away from the walls of the box in opposite corners. In each retention trial, the location of the novel versus the identical object was chosen randomly. Objects in the retention trial differed in both shape and color, and there was no overlap in objects seen by an individual animal at the adolescent and adult stage. Owing to the configurability of Lego-based object design and the standardization of object placement, the above approach represents an advance on traditional NORT protocols (132).

4.2.6 Chronic 2-photon imaging

Animals were habituated to a head-fixed position on a running wheel for 10 minutes two days before recording and for 20 minutes one day before recording. On the recording day, animals were lightly anesthetized (1.5% isoflurane for 3 minutes) to ease transfer to the wheel. Animals were allowed to recover for 15 minutes to minimize effects of residual isoflurane (22) and given water droplets to drink once every 0.5 – 1 hr to protect against dehydration. Arousal was measured with pupil tracking and wheel speed. Neural activity was recorded on a custom ThorLabs 2-photon imaging rig equipped with a tunable laser (Fianium, 830 nm) and a mouse running wheel. Incident light was attenuated with a Pockels cell and routed through the objective (16x, Olympus). X-y rastered videos (600 x 600 μm; 512 x 512 pixels; 30 fps) were collected in a single focal plane within layer II/III (150-250 μm ventral) to monitor cellular activity. Emitted light from neuronally-expressed YC2.60 (520 nm rest; 540 nm active) was collected via the objective. Emission wavebands were isolated by two dichroic mirrors and quantified by two photomultiplier tubes. Instrument signals was routed through a T9 board and synchronized (ThorSync) with simultaneously collected imaging data (ThorImage).

4.2.7 ROI extraction and spike deconvolution

YC2.60 FRET fluorescence amplitudes in the anti-correlated 520 nm and 540 nm wavebands were used to calculate the ratiometric time series $\Delta R/R$ for each pixel. Pyramidal cell somas were identified, neuropils were discarded, and motion artifacts were corrected with a custom image processing package (MATLAB). Spike deconvolution was performed with MLspike (133).

4.2.8 Avalanche identification

Neuronal avalanches were identified in each recording by grouping spikes from all ROIs into a time raster with temporal resolution $\Delta t = 33$ ms. Activations were defined either as inferred spikes or as suprathreshold spike probabilities (Fig. 4.2*B*, *red* and *green,* respectively), where the spike probability threshold θ varied between 0.001 and 0.01. Avalanches were defined as any series of consecutive time bins containing at least one activation flanked by time bins of silence on either side, and size was defined as the total number of spikes including reactivations, which are expected to be rare based on LFP analysis (2). Avalanche duration was defined as the number of time bins spanned by a cascade of consecutive activations. Size, duration, and mean-size-per-duration distributions were plotted in double-log coordinates to highlight scale-invariance (16). Avalanche size and duration power law slopes were tested against exponential and log-normal alternative distributions via the maximum log-likelihood ratio (LLR) and LLR significance was established using the method proposed by

Clauset (48).

4.3 Results

The perinatal PCP model is an established method for creating schizophrenia-like symptoms in rodents as evidenced by behavioral deficits, altered synaptic structure, and neurodynamical deviations from neurotypicality (20). To date, 19 adolescent mice and adult mice have been scored on the Novel Object Recognition Test (NORT) behavioral assay of episodic memory. Of these, one SAL-treated mouse and 4 PCP-treated mice expressing the FRET-based calcium indicator YC2.60 in superficial ACC were imaged while freely ambulating on a mouse wheel. Approximately 20 recordings of varying resolutions (300, 450, and 600 μm^2) lasting between 5 and 11 minutes each were collected with between 50 and 200 ROIs identified per field of view.

4.3.1 Preliminary results towards validation of the NORT memory assay

Avalanches have been observed in the brain, specifically in cortex, which is crucially involved in memory formation. This part of the brain has also been implicated in the pathobiology of schizophrenia. The Novel Object Recognition Test (NORT) is a non-rewarded paradigm focused on spontaneous exploratory behavior of rodents and requires memory traces of temporal order and object in place memory (Fig 4.1). Cohort sizes are currently insufficiently large to establish treatment group or sex differences.

4.3.2 Signatures of fractal organization and neuronal avalanches in spiking activity

Using two-photon imaging, we found dense labeling of cells expressing YC2.60 in layer II/III of cingulate cortex (Fig 4.2*A*). Fluorescence time series recorded in freely

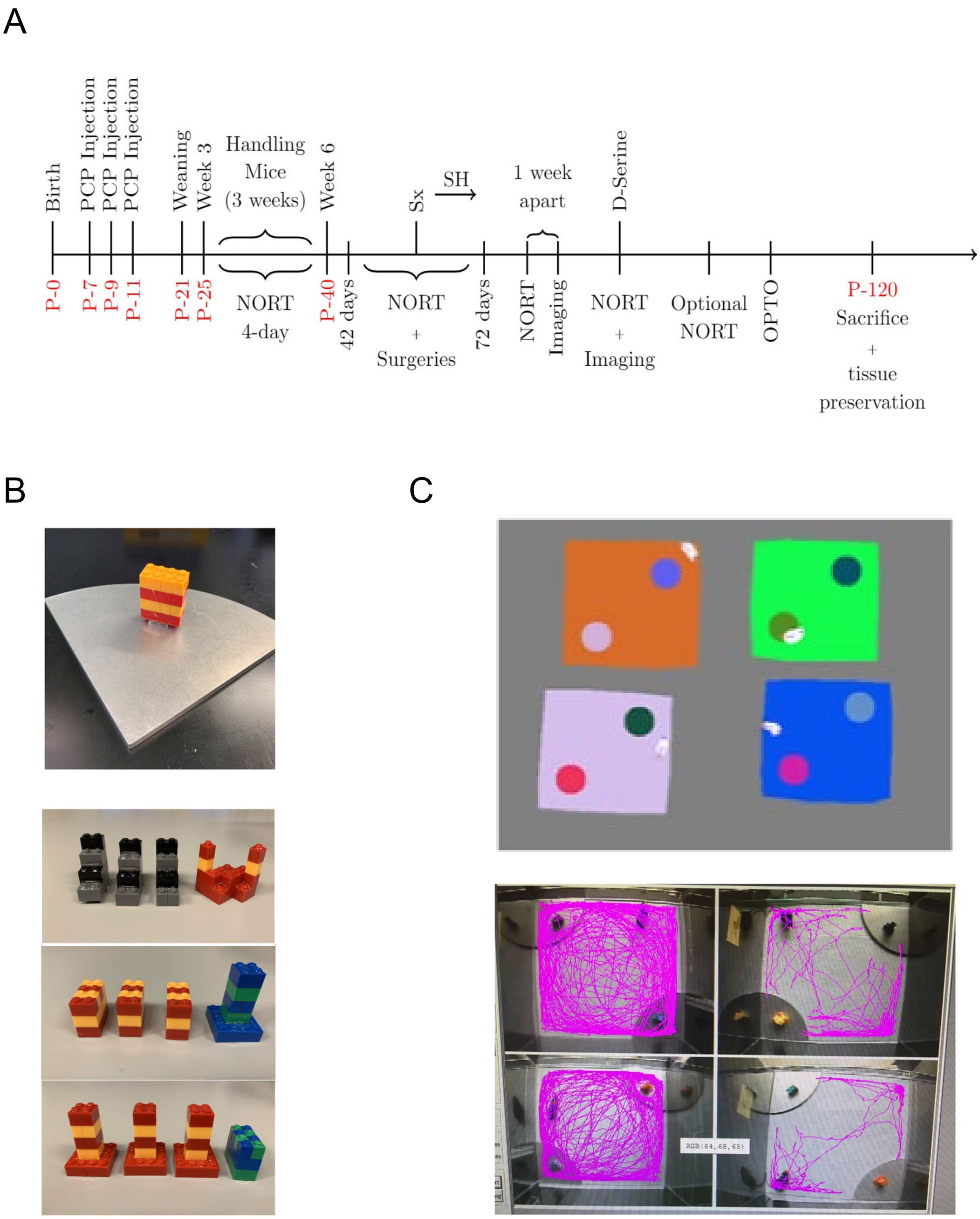

Figure 4.1: **Novel object recognition test of episodic memory in PCP-treated mice.** ***A***, Longitudinal experimental timeline for murine subjects showing drug treatments, surgery, adolescent behavioral testing, imaging, adult behavioral testing, drug rescue during behavior and imaging, optogenetic rescue during imaging, and histology. ***B***, Metal standardized object platform. *Lower:* Example sets of 4 objects (3 identical, 1 novel) used per mouse. ***C***, *Upper*:

TopScan visualization of 4 simultaneously recorded mice in individual plexiglass behavioral boxes. Colored square areas trace the floor of the box and circles span a 4 cm radius around objects. Mice are identified in white and tracked throughout the experiment. *Lower:* Animal location trace (*pink*) tracked over a 5 minute retention trial reveals that some mice explore the behavioral box and objects thoroughly (*left boxes)* while another mouse (*bottom right box)* exhibits signs of anxiety such as sitting in one spot, avoiding objects, and avoiding the open center of the box.

ambulating animals yielded ratiometric *ΔR/R* signal traces for each region of interest (ROI; purported cell bodies) which were deconvolved via MLspike into either Boolean spike times or a continuous spike rate estimate (Fig. 4.2*B*).

Tell-tale signatures of scale-free dynamics are evident in our preliminary data. We observe complex temporal organization, as shown in a ~2 minute snippet of *ΔR/R* fluorescence activity from a single ROI (Fig 4.3*A; upper, blue*) which exhibited ~5 significant departures from baseline with the largest activity burst located in the middle. The spike rate estimate trace (*lower, red*) shows that each of the bursts visible above is actually composed of a series of smaller bursts. This self-similarity was less clearly observed in the binary spiking time series (*green*).

We also observed self-similarity in the spatiotemporal patterning of the spiking raster for all cells in the field of view. Spike time rasters of drastically different durations (Fig. 4.4*B*; each a thin vertical slice of the raster above) exhibit statistically similar columnar (denoting spiking cascades e.g. avalanches) and horizontal (individual bursting cell) structural features across spatiotemporal scales.

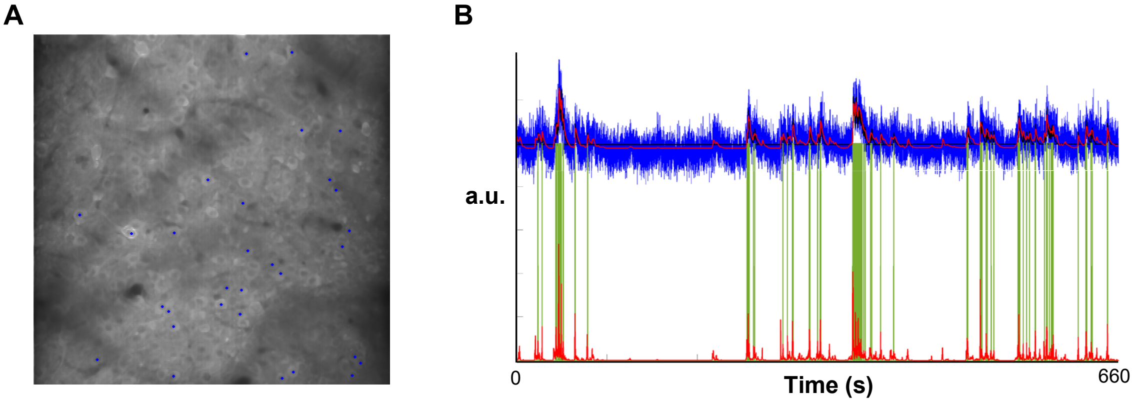

Figure 4.2: Two-photon imaging and spike deconvolution of neuronal activity in superficial ACC. ***A***, Ratiometric YC2.60 GECI signal in layer II/III neural tissue of anterior cingulate cortex (ACC) shows dense labeling of cells. Shadows are due to light scattering by blood vessels. Blue dots indicate cell soma centers found via automatic region-of-interest (ROI) registration. ***B***, Time series from a single ROI over a 11 minute recording in a freely ambulating animal. Ratiometric YC2.60 signal (*top, blue*) is first smoothed (*top, pink*) and then fit with a spike rate estimate (*bottom, red)* in MLspike. Alternatively, the ΔR/R signal was passed through MLspike deconvolution (*top, black)* to yield a binary spiking time series (*green*).

We tested for power laws in cascade size distributions. In a collection of data over all imaged mice, the cascade size probability approximately traced a power law distribution (Fig. 4.4*A*). The measured *P(S)* slope of -1.47 is in good agreement with the expected critical exponent α = 1.5. The cascade lifetime distribution approximately conformed to a power law with a slope of -1.09 (Fig. 4.4*B*), which is in poor agreement with the critical lifetime exponent β = 2. The mean-size-per-lifetime measure distributed along a power law with slope 1.22 (Fig. 4.4*C*). This is in only moderate agreement with the theoretical expectation that 1/συz = 2. Specifically, a slope of

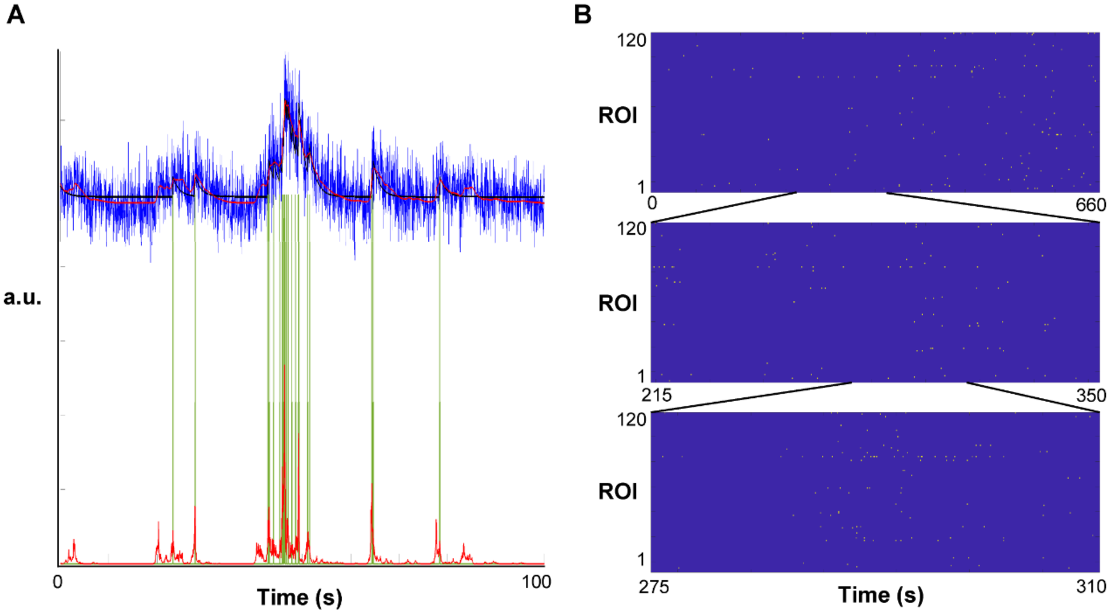

Figure 4.3: Preliminary evidence for self-similarity in the spatiotemporal organization of neuronal population activity. ***A***, A ~2 minute snippet of the ROI activity shown in Fig. 4.2*B*. Ratiometric YC2.60 signal (*top, blue*) and smoothed (*top, pink*) signal show ~5 significant departures from baseline with the largest activity burst located in the center. The spike rate estimate (*bottom, red)* reveals that each burst visible above is actually composed of a series of smaller bursts. The center burst specifically appears to be made up of 5 distinct smaller bursts, echoing the structure of the larger scale. This fractal quality is less clearly observed in the deconvolved spiking time series (*green*). ***B***, Spiking activity-time rasters of different durations (each a vertical slice of the raster above) exhibit similar columnar (denoting spiking cascades e.g. avalanches) and horizontal (individual bursting cell) structural qualities across spatiotemporal scales.

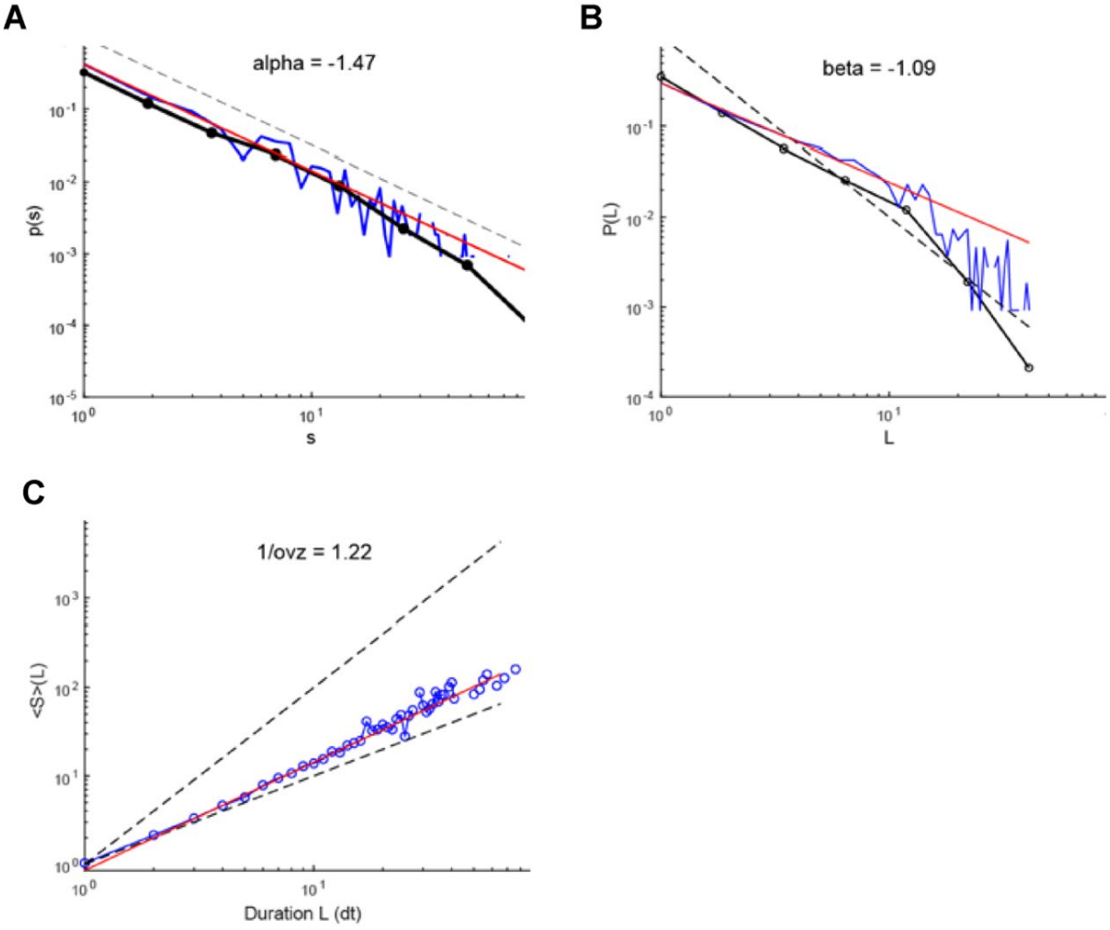

Figure 4.4: **Signatures of neuronal avalanches in freely moving SAL- and PCP-treated mice.** ***A***, In a collection of data over all imaged mice, the cascade size distribution approximately traces a power law distribution. The slope of -1.47 is in good agreement with the expected critical exponent α = -1.5. ***B***, The cascade lifetime distribution approximately conforms to a power law with a slope of -1.09, which is in poor agreement with the critical lifetime exponent β = -2. ***C***, The mean-size-per-lifetime distribution distribute along a power law with slope 1.22. This is in only moderate agreement with the theoretical expectation that 1/συz = 2. A slope of 1 implies minimally complex independent dynamics while a slope of 2 implies maximally complex e.g. critical dynamics.

$1/\sigma\upsilon z = 1$ implies minimally complex independent dynamics, while a slope of 2 implies maximally complex e.g. critical dynamics (Fig. 4.4*C, dotted lines*).

4.4 Discussion

Cognitive function impairment is a primary and persistent manifestation in patients with schizophrenia (134). Previous research has pointed to GABAergic signaling dysfunction as a cause of positive and negative symptoms, but the specific population-level manifestations of disturbed neuronal activity patterns are unknown. A recent study (20) implementing perinatal exposure to the NMDA receptor antagonist phencyclidine (PCP), a well-established method of eliciting schizophrenia-like symptomatology in rodents, revealed altered neuronal avalanche characteristics in adolescent rats. We propose that observing neural activity while manipulating inhibitory cell ensembles may reveal insight into the disorganized cortical dynamics and behavioral deficits exhibited by adult mice treated perinatally with PCP. Using two-photon calcium imaging and optogenetics in PV-Cre, SST-Cre, and VIP-Cre transgenic mouse lines, we hope to demonstrate that neuronal avalanche analysis can reveal precise, cell type-specific contributions to network dysfunction.

In the preceding Chapters, we present the argument that the healthy neural state in mammalian cortex is scale-invariant dynamics characterized by a balance between excitatory (glutamatergic) and inhibitory (GABAergic) contributions to collective spiking activity. To characterize what is altered in cortical networks in a developmental mouse model for schizophrenia, we analyze neuronal population activity via multiphoton calcium imaging. We make a number of methodological advances on previous work on avalanche dynamics during schizophrenia in rodents: previous work was done on rats, entailing a limited selection of transgenic Cre lines, as well as constraints around the developmental stage and behavioral state of the animal during imaging. Specifically, previous neuronal monitoring was conducted on lightly anesthetized adolescent rats whereas our work is conducted in and awake and behaving adult mice. This is an important aspect of our experimental design, as neuronal avalanches have been shown to be sensitive to anesthesia (22, 135).

4.4.1 Distortion of neural circuits in schizophrenia

Schizophrenia often manifests during adolescence, when the brain is still in maturation. This has led to the idea that schizophrenia might have a strong developmental component which should adequately be addressed in animal models for schizophrenia. It is for that reason that we focused here on the developmental PCP model in which the NMDA receptor is being affected early on. This receptor is implicated in controlling the structure and plasticity of developing brain circuitry. Exposure to NMDA receptor antagonist PCP in late fetal/early postnatal periods in rodent increases death of neurons by apoptosis (136), whereas acute administration of PCP in adulthood damages cortex via different cellular mechanisms, namely necrosis followed by gliosis (117, 137, 138). The expression of cytoskeleton proteins is also altered in a MK801 NMDAR antagonist study (139), an alteration which may cause disorganization of circuits in adulthood. Prenatal administration of MK801 decreased the PV neuron population in medial cortex, including ACC (140), which is also observed in schizophrenic patients (141).

Another mechanism of prefrontal cortical dysfunction that is recapitulated in the PCP glutamatergic hypofunction model is a series of knock-on effects caused by reduced activity-driven expression of GAD67 (111). GAD67 is a crucial protein for the synthesis of GABA in cortex, which in adult patients is reduced by 50% in PV axons (110, 142). There is also a layer III pyramidal cell reduction of the $\mathrm{GABA_A}$ receptor (143) that registers inputs from PV basket cells; this has been interpreted as a main mechanism in the pathological attenuation of gamma activity (106, 114). Reduced expression of the Kv9.3 potassium channel alpha-subunit (144), which serves to delay the fast EPSP decay in PV interneurons (145), might be yet another mechanism for reduced gamma power as it causes a loss of temporal precision in PV cells (7). Maturation studies point to vulnerable periods where interruptions to normal development could affect the number of PV chandelier cell synaptic terminals or the efficacy of PV basket cell terminals (146).

From a circuit perspective, PV cells inhibit mostly each other and excitatory pyramidal cells (PYR), while SST cells inhibit PYR, PV, and VIP cells. SST cell receptors are also altered in schizophrenia (147). Currently it is not known how avalanche dynamics in cortex are affected by alterations in activity among these three GABAergic cell types. To underscore the complexity of these processes: a single interneuron might inhibit many dendrites on a given Pyr cell, or only those a single dendritic branch, or only innervate a small subregion of one branch. For example, in M1 a single dendritic process may receive excitatory inputs organized such that synapses associated with different motor skills cluster on different dendritic branches (148). Therefore, disinhibiting a specific dendritic branch or subregion may permit reorganization or refinement of one skill while leaving other learned motor processes undisturbed. This suggests that synaptic network malformations seen in schizophrenia may cause abnormal network dynamics associated with a broad set of cognitive and behavioral impairments.

4.4.2 Future directions

Recent research (20) has suggested that aberrant neural dynamics in schizophrenia may be detected by calculating the critical branching parameter, σ, defined as the average ratio of the number of descendants to ancestors within a cascade, which captures the balance between stable propagation ($\sigma=1$), explosive activity ($\sigma>1$, sometimes referred to as the *epileptic regime*), and signal die-out ($\sigma<1$). Altered spiking and avalanche dynamics in lightly-anaesthetized PCP-treated rats were detected by calculating σ_{repeat}, a measure of repeat activations by individual ROIs within a single avalanche. We will explore this measure in data recorded from awake PCP-treated mice.

We will also test the specific hypotheses that neural and behavioral deficits will be rescued by acute administration of D-serine (149), and that optogenetic stimulation of PV and SST interneurons using the depolarizing opsin NpHR (AAV-EF1aDIO-eNpHR3.0-mCherry, UNC Vector Core) will alter or improve cortical activity without fully recovering neurotypical dynamics. The goal of our study is to characterize the breakdown of precisely coordinated neural activity in superficial cortex, the locus of both avalanche dynamics and cognition, which are disturbed in schizophrenia.

Chapter 5: Summary and Discussion

Since the discovery of neuronal avalanches by Beggs & Plenz in 2003, the critical brain hypothesis has gained increasing traction among researchers who study neural excitation/inhibition (E/I) balance and mesoscale cortical activity in health and disease. A current focus of investigation is the role of different cortical circuit components for maintaining, modulating, and leveraging the flexibility and information processing benefits associated with phase transition-adjacent dynamics. However, it remains to be seen whether the most promising predictions of critical systems theory are applicable to neuronal activity, and while there is an important role for theoretical and simulation-based exploration of critical systems in the brain, the shortest path to translationally-relevant knowledge is via experimentation *in vivo.* Awake and behaving rodent and nonhuman primate models of human disease permit the use of invasive techniques to precisely monitor electrophysiological and biophysical measures. In these animal models, recent development of light-mediated perturbation of excitable cells allow the experimenter to optogenetically manipulate activity in specific cell types to elucidate their influence on circuit function and avalanche organization. Using these techniques and avalanche analysis, progress can be made towards establishing a cohesive framework for understanding activity among cortical neurons.

5.1 Summary

By combining electrophysiology, calcium imaging and optogenetics, as well as behavioral testing and neural network analysis, we confirm previous findings that superficial cortex operates close to a critical state in a stable manner over days and weeks. Importantly, we demonstrate the scale-invariance in avalanche temporal shape and scaling relationships predicted from the theory of critical dynamics. We successfully integrated the apparent dichotomy of scale-independent avalanches with scale-dependent neuronal oscillations exemplified using beta/gamma-oscillations. We further propose that in an animal model for schizophrenia, a brain disease characterized by aberrant E/I balance and impaired cognition, measures of population activity may deviate from criticality. On the basis of these results and existing literature, we conclude that critical systems theory is likely to offer valuable insights and improvements to traditional neuroscientific practice with implications for translational and clinical research.

In Chapter 2, we studied the stability of network structure and dynamics. We found that local field potentials in nonhuman primate displayed characteristic correlation networks and avalanche dynamics in a stable manner over days and weeks. The influence of common input to electrodes was removed via the Normalized Count network reconstruction (68), which permitted us to identify a stable integrative network organization that captured the essence of how avalanches unfold in space and time in the brain.

In Chapter 3, we leveraged the full nonhuman primate data volume (>20 hr) to attain precise statistics on even large and rare cascades. Testing the prediction from critical systems theory that avalanche shapes should be scale-invariant (52), we applied the renormalization shape collapse function to avalanches in nonhuman primate field potentials. We discovered that avalanches *in vivo* obeyed the shape collapse at short and long timescales, yet failed to display scale-invariant profiles at intermediate timescales impacted by spontaneous synchronized oscillations. This entirely novel characterization of population coordination may represent a new biomarker for cortical synchrony along both the critical axis (E/I balance) as well as the power-frequency dimension with potential for capturing cross-frequency coupling. Finally, we showed that removing the dominant 30 Hz oscillation via a high-order bandpass filter simultaneously destroyed signatures of criticality, suggesting that avalanches and oscillations are not independent processes occurring orthogonally to each other (a simple superposition), but instead together define the healthy state of the mammalian brain.

In Chapter 4, we presented preliminary data towards detecting aberrant avalanche and network dynamics in a developmental mouse model for schizophrenia. Combining behavioral assays of episodic memory with multi-photon calcium imaging and optogenetics in PV-, SST-, and VIP-Cre transgenic mouse lines, we presented initial work towards establishing impaired episodic memory and deviations from criticality in neuronal activity of PCP-treated mice. These results represent progress towards our specific aim of characterizing the inhibition-mediated breakdown of precisely coordinated activity in cortical layer II/III.

5.2 Discussion

5.2.1 Supporting evidence for critical brain dynamics

Criticality in cortical dynamics seems both increasingly likely and increasingly important. The results presented in this dissertation demonstrate that over weeks in nonhuman primates, avalanche activity is stable, as is integrative network organization. We have also confirmed the prediction that temporal profile renormalization can apply to neural activity and, importantly, we find that oscillations are crucial in shaping neuronal avalanches. Further, we have shown progress towards characterizing aberrations of critical brain dynamics caused by disease.

The current work supports the hypothesis that the brain operates close to a critical point balanced at a phase transition between global synchrony and purely Poisson independence, i.e. between explosive, invariably system-spanning cascades and dampened, inconsequential blips of activity. This finding has particular import in neural systems, which are information processing organs crucial for survival. Therefore, disorders of the brain may be better understood as the loss of precisely controlled, transient deviations from criticality. Indeed, evolution has selected for increased cognition (105, 150), and initial reports suggest that sustained deviations from criticality are principally observed in brain states associated with the loss of cognitive capacity, i.e. in pathology and non-alert states of consciousness (20, 22, 25, 28, 62, 65).

Taken together, these data illustrate a system where avalanches are usually occurring, yet locally interrupted by oscillations. This can be considered advantageous in the context of information processing, because the pink noise “crackle” (35) of avalanching will, when necessary, give way to the collective "strum" of a neuronal oscillation. Avalanching is conducive to the active maintenance of an optimally resonant network state (60) comprised of a near-threshold neuronal population (151). An avalanche "default mode" could permit incident oscillations to propagate in an energetically efficient manner and facilitate forgetting of irrelevant information (13).

5.2.2 A role for theory

When conducting research in a new field, it is necessary to make empirical observations so that our scientific designs and conclusions may be well-founded. Further experimental and theoretical work will produce a more precise framework for exploration of critical brain dynamics.

For example, higher-order interactions in cortical activity could be captured by the "Dichotomized Gaussian" (DG) model which was shown to outperform the Ising model in prediction of both second- and third-order functional correlations (62). In this model, drift in the mean correlation strength results in a loss of avalanche organization. Tuning the average strength tunes the dynamics towards either subcritical or supercritical avalanche size distributions. The DG model is especially relevant to the Chapter 2 investigation of critical dynamics on cortical functional networks because it offers a minimal model capturing both critical dynamics and correlations, while permitting manipulation of the critical branching parameter σ. This could be used to model how a miscalibrated homeostasis might cause the loss of scale-invariant dynamics (or a departure from the optimal quasi-critical state/Griffith's region (152)).

5.2.3 Unresolved questions

Where does information live in the brain? Is it “hard-coded” in synaptic architecture? Or is information principally found in the ever-changing ensembles of electrical spikes propagated among neuronal populations?

A common problem in schizophrenic patient care is that patient records often begin at hospital admission for acute psychosis without the context of measurements in prodromal or preclinical brain states, making it difficult to detect disease-specific signatures of brain activity. Could avalanche shapes be used to distinguish between healthy and disease states in general, or perhaps even between healthy and trending-towards-unhealthy states in the same animal or subject?

Could neuronal avalanche shapes be used as a new lens to understand brain activity across temporal scales? Will critical brain dynamics have relevance for the issue of how the brain filters out unattended information while accentuating salient signals (also known as the “binding problem”)? Could this problem be better understood through a theory of cortex inclusive of criticality?

What will be the impact of technologies built upon the critical brain framework? Can scientists take inspiration from how the brain works when it comes to domains such as machine learning, neuromorphic engineering, and the development of brain-computer interface (BCI) technology?

5.3 Directions for future work

5.3.1 Translational research in neuronal avalanche shape analysis

Retooling requirements (153) are a barrier to entry for new types of analysis. In this regard, neuronal avalanche research is advantaged; it so far does not require new types of tools. Instead, familiar data can be looked at with established methods and still produce new science. In this section we consider two possibilities for the incorporation of critical brain dynamics into psychiatric and neurological health care.

Just as patients today may be fitted with EEG caps for real-time noninvasive monitoring of oscillatory signals, one possible scenario is that existing neural observation methods (EEG, MEG, ECoG) will be used to assess avalanche structures as a complementary technique. We anticipate that there may be characteristic deformations of avalanche organization associated with specific diseases (25), and that this developing technique will produce novel neurologically-based biomarkers (e.g. avalanche shape analysis) with both diagnostic and prognostic value.

A second possibility is avalanche analysis as a complement for transcranial magnetic stimulation (TCMS), which could be considered a natural pairing. Akin to tests of critical slowing down (50), the purpose of TCMS is to provide a “kick” to a specific region of brain. As a system measure, avalanche analysis has already been shown to be effective for evaluating network excitability (susceptibility) in response to perturbation (28).

5.3.2 Integrating paradigms

How do we ask questions about the functioning of a system? Intellectual structures through which productive inquiry proceeds is essentially the definition of a scientific paradigm, a concept popularized by Thomas Kuhn (153). Kuhn described how “normal” science is done in the context of a given paradigm. This paradigm is comprised of a set of exemplary tools, methods, concepts and theories which become interrupted if and when “anomalies” are recognized to such an extent that new frameworks are constructed to explain new facts.

Any given theory can be considered incomplete, so there is often a collection of anomalies (i.e. $1/f$ crackling noise, neuronal avalanches, inverted U-profiles, critical slowing down, diverging correlations, etc.) which can be brought together and explained within some new framework (e.g. critical brain dynamics) in an advance which is able to resolve new findings with what was previously known and expected.

However, there has been some contention around whether the brain really is critical (90). Healthy skepticism is particularly crucial and appropriate at an early point along the development of a scientific framework. Some have said, “brain activity may resemble criticality, but it is not truly critical dynamics you are observing”, and this remains a possibility. How can experimentalists empirically respond to skeptics? Although there are many possible directions (see Chapter 3 re: parabolic vs semicircle shape motifs), one thing is clear: we in neuroscience should continue to explore the applicability of a deep body of physics under development for the better part of a century (17, 36, 154, 155).

To articulate a paradigm for cortex inclusive of criticality, it will be necessary to resolve residual ambiguities and refine an integrated framework. Persuasive arguments will be developed if the new framework predicts phenomena previously unsuspected. This could include the identification of universal constants including, perhaps, those hinted at in the intrinsic log spacing of brain wave bands (156). There may also be the development of quantitative laws, like those describing how the specific biology of neural systems constrains the breadth of scale over which the physics in question applies.

5.3.3 The search for the substrate of thought

Scientists and philosophers have attempted to formulate the question of how the brain can house the mind. We suggest the question be asked in this way: “What is the substrate upon which thought unfolds?” Given the current work and related research, we would like to put forward the hypothesis that that substrate might be avalanches. The critical state may be a “dial tone” signaling readiness for communication, and neuronal avalanches may be the energetic medium through which other dynamical structures unfold and against which they can be distinguished.

Unperturbed, critical dynamics represents a maximally variable network state in the presence of correlations among network components. Though seemingly stochastic on the microscale, critical phenomena reliably conform to distinct statistical trends over long observation times. However, these distinct tendencies currently do not offer predictive power *per se* (similar to how earthquakes cannot reliably be predicted). Therefore, signals that occur in a temporally reliable manner, e.g. neuronal oscillations, can be distinguished as salient against differently organized activity.

Given that neuronal avalanches and oscillations co-exist and that their temporal domains are anti-correlated (c.f. Fig. 3.4*G*; frontal cortex of nonhuman primate), it may be possible to consider these two dynamics as computationally synergistic. We therefore propose that avalanche organization constitutes a *fabric* we call the **critical manifold**. The manifold surface may be best approximated by the sloping contours of

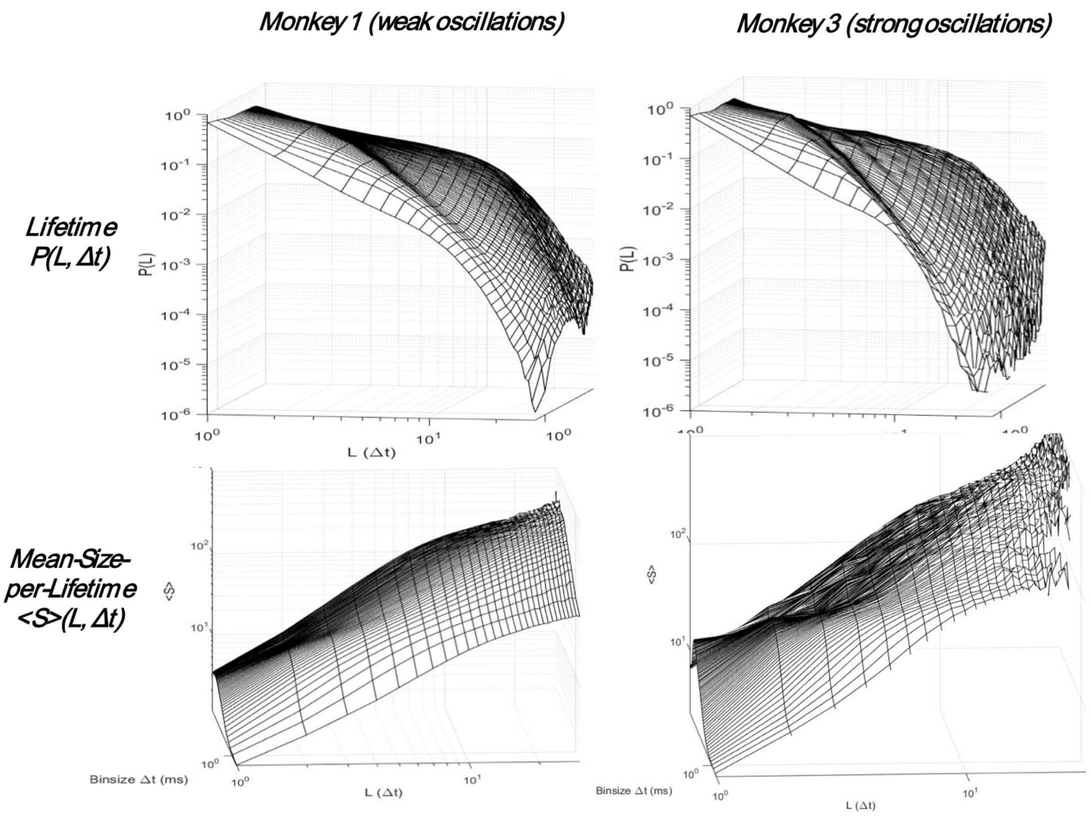

Figure 5.1: Neuronal avalanche lifetime-probability-per-Δt and mean-size-per-lifetime-per- Δt distributions in NHP reveal a "fabric" marked by wrinkles in time. Traditional power law measures of empirical brain data are explored across temporal scale. Characteristic "wrinkles" visible as pronounced topographical features were found in a monkey with strong 30 Hz brain waves (*top right, bottom right*), but were missing in a monkey with weak oscillations (*top left, bottom left*).

the triple-logarithmic $\langle S \rangle$-per-L-per-Δt distribution (Fig. 5.1, *bottom row*). Just as power-frequency peaks of physiological oscillations will approximate a Gaussian shape only when plotted in log axes (c.f. Fig. 3.4*E*), the critical manifold similarly speaks to a logarithmic coordinate system transcending scale.

In the spirit of speculation, perhaps the brain itself leverages renormalization. This would allow neural systems to efficiently monitor deviations from a “pure” criticality which is complex but not meaningful (because critical dynamics emerges from the local interaction of network elements, i.e. only bottom-up influences). Instead, other organizational schemes such as rate codes, temporal codes, and network oscillations may impart somewhat-but-not-fully orthogonal structure onto the avalanching substrate, thereby manipulating the fabric of the critical manifold.

Bibliography

1. Pajevic S, Plenz D (2012) The organization of strong links in complex networks. *Nat Phys* 8(5):429-436.
2. Yu S, Klaus A, Yang HD, Plenz D (2014) Scale-Invariant Neuronal Avalanche Dynamics and the Cut-Off in Size Distributions. *Plos One* 9(6).
3. Consortium TWWMHS (2004) Prevalence, Severity, and Unmet Need for Treatment of Mental Disorders in the World Health Organization World Mental Health Surveys. *JAMA* 291(21):2581-2590.
4. Groiss SJ, Wojtecki L, Südmeyer M, Schnitzler A (2009) Review: Deep brain stimulation in Parkinson's disease. *Therapeutic Advances in Neurological Disorders* 2(6):379-391.
5. Beggs JM, Plenz D (2003) Neuronal avalanches in neocortical circuits. *J Neurosci* 23(35):11167-11177.
6. Kopell N, Ermentrout GB, Whittington MA, Traub RD (2000) Gamma rhythms and beta rhythms have different synchronization properties. *Proceedings of the National Academy of Sciences* 97(4):1867-1872.
7. Gonzalez-Burgos G, Lewis DA (2008) GABA neurons and the mechanisms of network oscillations: Implications for understanding cortical dysfunction in schizophrenia. *Schizophrenia Bull* 34(5):944-961.
8. Buzsáki G, Logothetis N, Singer W (2013) Scaling Brain Size, Keeping Timing: Evolutionary Preservation of Brain Rhythms. *Neuron* 80(3):751-764.
9. Tort ABL, Komorowski R, Eichenbaum H, Kopell N (2010) Measuring Phase-Amplitude Coupling Between Neuronal Oscillations of Different Frequencies. *J Neurophysiol* 104(2):1195-1210.
10. Krueger JM*, et al.* (2008) Sleep as a fundamental property of neuronal assemblies. *Nat Rev Neurosci* 9:910.
11. Fries P, Nikolić D, Singer W (2007) The gamma cycle. *Trends Neurosci* 30(7):309-316.
12. Gireesh ED, Plenz D (2008) Neuronal avalanches organize as nested theta- and beta/gamma-oscillations during development of cortical layer 2/3. *Proceedings of the National Academy of Sciences* 105(21):7576-7581.

13. Lundqvist M, Herman P, Warden MR, Brincat SL, Miller EK (2018) Gamma and beta bursts during working memory readout suggest roles in its volitional control. *Nat Commun* 9.

14. Bieler M*, et al.* (2017) Rate and Temporal Coding Convey Multisensory Information in Primary Sensory Cortices. *eneuro* 4(2):ENEURO.0037-0017.2017.

15. Singer W (1999) Neuronal Synchrony: A Versatile Code for the Definition of Relations? *Neuron* 24(1):49-65.

16. Klaus A, Yu S, Plenz D (2011) Statistical Analyses Support Power Law Distributions Found in Neuronal Avalanches. *Plos One* 6(5).

17. Bak P, Tang C, Wiesenfeld K (1987) Self-organized criticality: An explanation of the 1/f noise. *Physical Review Letters* 59(4):381-384.

18. Voytek B*, et al.* (2015) Age-Related Changes in 1/f Neural Electrophysiological Noise. *The Journal of Neuroscience* 35(38):13257-13265.

19. Awh E, Belopolsky AV, Theeuwes J (2012) Top-down versus bottom-up attentional control: a failed theoretical dichotomy. *Trends in Cognitive Sciences* 16(8):437-443.

20. Seshadri S, Klaus A, Winkowski DE, Kanold PO, Plenz D (2018) Altered avalanche dynamics in a developmental NMDAR hypofunction model of cognitive impairment. *Transl Psychiat* 8.

21. Hahn G*, et al.* (2010) Neuronal avalanches in spontaneous activity in vivo. *J Neurophysiol* 104(6):3312-3322.

22. Bellay T, Klaus A, Seshadri S, Plenz D (2015) Irregular spiking of pyramidal neurons organizes as scale-invariant neuronal avalanches in the awake state. *Elife* 4.

23. Yu S*, et al.* (2017) Maintained avalanche dynamics during task-induced changes of neuronal activity in nonhuman primates. *Elife* 6.

24. Meisel C, Olbrich E, Shriki O, Achermann P (2013) Fading Signatures of Critical Brain Dynamics during Sustained Wakefulness in Humans. *J Neurosci* 33(44):17363-17372.

25. Shriki O*, et al.* (2013) Neuronal Avalanches in the Resting MEG of the Human Brain. *J Neurosci* 33(16):7079-7090.

26. Shriki O (2014) Neuronal avalanches in human MEG and EEG. *J Mol Neurosci* 53:S116-S116.

27. Fekete T*, et al.* (2018) Critical dynamics, anesthesia and information integration: Lessons from multi-scale criticality analysis of voltage imaging data. *Neuroimage* 183:919-933.

28. Meisel C*, et al.* (2015) Intrinsic excitability measures track antiepileptic drug action and uncover increasing/decreasing excitability over the wake/sleep cycle. *P Natl Acad Sci USA* 112(47):14694-14699.

29. Arviv O, Medvedovsky M, Sheintuch L, Goldstein A, Shriki O (2016) Deviations from Critical Dynamics in Interictal Epileptiform Activity. *J Neurosci* 36(48):12276-12292.

30. Iyer KK*, et al.* (2015) Cortical burst dynamics predict clinical outcome early in extremely preterm infants. *Brain* 138:2206-2218.

31. Roberts JA, Iyer KK, Finnigan S, Vanhatalo S, Breakspear M (2014) Scale-Free Bursting in Human Cortex following Hypoxia at Birth. *J Neurosci* 34(19):6557-6572.

32. di Santo S, Villegas P, Burioni R, Muñoz MA (2018) Landau–Ginzburg theory of cortex dynamics: Scale-free avalanches emerge at the edge of synchronization. *Proceedings of the National Academy of Sciences* 115(7):E1356-E1365.

33. Priesemann V*, et al.* (2014) Spike avalanches in vivo suggest a driven, slightly subcritical brain state. *Front Syst Neurosci* 8.

34. Lombardi F, Herrmann HJ, Plenz D, De Arcangelis L (2014) On the temporal organization of neuronal avalanches. *Front Syst Neurosci* 8(204).

35. Sethna JP, Dahmen KA, Myers CR (2001) Crackling noise. *Nature* 410(6825):242-250.

36. Wilson KG (1983) The renormalization group and critical phenomena. *Reviews of Modern Physics* 55(3):583-600.

37. Fisher ME (1974) The renormalization group in the theory of critical behavior. *Reviews of Modern Physics* 46(4):597-616.

38. Munoz MA, Dickman R, Vespignani A, Zapperi S (1999) Avalanche and spreading exponents in systems with absorbing states. *Phys Rev E* 59(5):6175-6179.

39. Harris TE (1963) *The theory of branching processes* (Springer, Berlin,) pp xiv, 230 p.

40. Pérez-Reche FJ, Vives E (2003) Finite-size scaling analysis of the avalanches in the three-dimensional Gaussian random-field Ising model with metastable dynamics. *Physical Review B* 67(13):134421.

41. Bak P (1997) How Nature Works: The Science of Self-Organized Criticality. *American Journal of Physics* 65(6):579-580.

42. Herz AVM, Hopfield JJ (1995) Earthquake Cycles and Neural Reverberations: Collective Oscillations in Systems with Pulse-Coupled Threshold Elements. *Physical Review Letters* 75(6):1222-1225.

43. Chen D-M, Wu S, Guo A, Yang ZR (1995) Self-organized criticality in a cellular automaton model of pulse-coupled integrate-and-fire neurons. *Journal of Physics A: Mathematical and General* 28(18):5177-5182.

44. Corral Á, Pérez CJ, Díaz-Guilera A, Arenas A (1995) Self-Organized Criticality and Synchronization in a Lattice Model of Integrate-and-Fire Oscillators. *Physical Review Letters* 74(1):118-121.

45. Eurich CW, Herrmann JM, Ernst UA (2002) Finite-size effects of avalanche dynamics. *Phys Rev E* 66(6):066137.

46. Markram H*, et al.* (2015) Reconstruction and Simulation of Neocortical Microcircuitry. *Cell* 163(2):456-492.

47. Poil S-S, Hardstone R, Mansvelder HD, Linkenkaer-Hansen K (2012) Critical-state dynamics of avalanches and oscillations jointly emerge from balanced excitation/inhibition in neuronal networks. *The Journal of neuroscience : the official journal of the Society for Neuroscience* 32(29):9817-9823.

48. Clauset A, Shalizi CR, Newman MEJ (2009) Power-Law Distributions in Empirical Data. *Siam Rev* 51(4):661-703.

49. McNally JM, McCarley RW (2016) Gamma band oscillations: a key to understanding schizophrenia symptoms and neural circuit abnormalities. *Current Opinion in Psychiatry* 29(3):202-210.

50. Meisel C, Klaus A, Kuehn C, Plenz D (2015) Critical Slowing Down Governs the Transition to Neuron Spiking. *Plos Comput Biol* 11(2):e1004097.

51. Yu S, Yang H, Shriki O, Plenz D (2013) Universal organization of resting brain activity at the thermodynamic critical point. *Front Syst Neurosci* 7.

52. Friedman EJ, Landsberg AS (2013) Hierarchical networks, power laws, and neuronal avalanches. *Chaos* 23(1):013135.

53. Marder E, Goaillard JM (2006) Variability, compensation and homeostasis in neuron and network function. *Nat Rev Neurosci* 7(7):563-574.

54. Lutcke H, Margolis DJ, Helmchen F (2013) Steady or changing? Long-term monitoring of neuronal population activity. *Trends Neurosci* 36(7):375-384.

55. Petermann T*, et al.* (2009) Spontaneous cortical activity in awake monkeys composed of neuronal avalanches. *P Natl Acad Sci USA* 106(37):15921-15926.

56. Kinouchi O, Copelli M (2006) Optimal dynamical range of excitable networks at criticality. *Nat Phys* 2(5):348-352.

57. Shew WL, Yang HD, Yu S, Roy R, Plenz D (2011) Information Capacity and Transmission Are Maximized in Balanced Cortical Networks with Neuronal Avalanches. *J Neurosci* 31(1):55-63.

58. Gautam H, Hoang TT, McClanahan K, Grady SK, Shew WL (2015) Maximizing Sensory Dynamic Range by Tuning the Cortical State to Criticality. *Plos Comput Biol* 11(12).

59. Shew WL, Yang HD, Petermann T, Roy R, Plenz D (2009) Neuronal Avalanches Imply Maximum Dynamic Range in Cortical Networks at Criticality. *J Neurosci* 29(49):15595-15600.

60. Yang HD, Shew WL, Roy R, Plenz D (2012) Maximal Variability of Phase Synchrony in Cortical Networks with Neuronal Avalanches. *J Neurosci* 32(3):1061-1072.

61. Karimipanah Y, Ma ZY, Miller JEK, Yuste R, Wessel R (2017) Neocortical activity is stimulus- and scale-invariant. *Plos One* 12(5).

62. Yu S*, et al.* (2011) Higher-Order Interactions Characterized in Cortical Activity. *J Neurosci* 31(48):17514-17526.

63. Tagliazucchi E, Balenzuela P, Fraiman D, Chialvo DR (2012) Criticality in large-scale brain fMRI dynamics unveiled by a novel point process analysis. *Front Physiol* 3.

64. Fraiman D, Chialvo DR (2012) What kind of noise is brain noise: anomalous scaling behavior of the resting brain activity fluctuations. *Front Physiol* 3.

65. Stewart CV, Plenz D (2008) Homeostasis of neuronal avalanches during postnatal cortex development in vitro. *J Neurosci Meth* 169(2):405-416.

66. Tetzlaff C, Okujeni S, Egert U, Worgotter F, Butz M (2010) Self-Organized Criticality in Developing Neuronal Networks. *Plos Comput Biol* 6(12).

67. Watts DJ, Strogatz SH (1998) Collective dynamics of 'small-world' networks. *Nature* 393(6684):440-442.

68. Pajevic S, Plenz D (2009) Efficient Network Reconstruction from Dynamical Cascades Identifies Small-World Topology of Neuronal Avalanches. *Plos Comput Biol* 5(1).

69. Kreindler GE, Young HP (2014) Rapid innovation diffusion in social networks. *Proceedings of the National Academy of Sciences* 111(Supplement 3):10881-10888.

70. Pastor-Satorras R, Castellano C, Van Mieghem P, Vespignani A (2015) Epidemic processes in complex networks. *Reviews of Modern Physics* 87(3):925-979.

71. De Domenico M, Granell C, Porter MA, Arenas A (2016) The physics of spreading processes in multilayer networks. *Nat Phys* 12:901.

72. Alstott J, Pajevic S, Bullmore E, Plenz D (2015) Opening bottlenecks on weighted networks by local adaptation to cascade failures. *J Complex Netw* 3(4):552-565.

73. Gleeson JP, Durrett R (2017) Temporal profiles of avalanches on networks. *Nat Commun* 8(1):1227.

74. Scott G*, et al.* (2014) Voltage Imaging of Waking Mouse Cortex Reveals Emergence of Critical Neuronal Dynamics. *The Journal of Neuroscience* 34(50):16611-16620.

75. Ponce-Alvarez A, Jouary A, Privat M, Deco G, Sumbre G (2018) Whole-Brain Neuronal Activity Displays Crackling Noise Dynamics. *Neuron* 100(6):1446-1459.e1446.

76. Solovey G, Miller K, Ojemann J, Magnasco M, Cecchi G (2012) Self-Regulated Dynamical Criticality in Human ECoG. *Frontiers in Integrative Neuroscience* 6(44).

77. Palva JM*, et al.* (2013) Neuronal long-range temporal correlations and avalanche dynamics are correlated with behavioral scaling laws. *Proceedings of the National Academy of Sciences* 110(9):3585-3590.

78. Cocchi L, Gollo LL, Zalesky A, Breakspear M (2017) Criticality in the brain: A synthesis of neurobiology, models and cognition. *Progress in Neurobiology* 158:132-152.

79. Hesse J, Gross T (2014) Self-organized criticality as a fundamental property of neural systems. *Front Syst Neurosci* 8(166).

80. Plenz D (2012) Neuronal Avalanches and Coherence Potentials. *Eur Phys J Spec Top*: 205: 259.

81. Chialvo DR (2010) Emergent complex neural dynamics. *Nat Phys* 6:744.

82. de Arcangelis L, Perrone-Capano C, Herrmann HJ (2006) Self-Organized Criticality Model for Brain Plasticity. *Physical Review Letters* 96(2):028107.

83. West BJ, Geneston EL, Grigolini P (2008) Maximizing information exchange between complex networks. *Phys Rep* 468(1-3):1-99.

84. Rybarsch M, Bornholdt S (2014) Avalanches in Self-Organized Critical Neural Networks: A Minimal Model for the Neural SOC Universality Class. *Plos One* 9(4):e93090.

85. Laurson L*, et al.* (2013) Evolution of the average avalanche shape with the universality class. *Nat Commun* 4:2927.

86. Papanikolaou S*, et al.* (2011) Universality beyond power laws and the average avalanche shape. *Nat Phys* 7:316.

87. Friedman N*, et al.* (2012) Universal Critical Dynamics in High Resolution Neuronal Avalanche Data. *Physical Review Letters* 108(20):208102.

88. Shaukat A, Thivierge J-P (2016) Statistical Evaluation of Waveform Collapse Reveals Scale-Free Properties of Neuronal Avalanches. *Frontiers in Computational Neuroscience* 10(29).

89. Dalla Porta L, Copelli M (2019) Modeling neuronal avalanches and long-range temporal correlations at the emergence of collective oscillations: Continuously varying exponents mimic M/EEG results. *Plos Comput Biol* 15(4):e1006924.

90. Touboul J, Destexhe A (2017) Power-law statistics and universal scaling in the absence of criticality. *Phys Rev E* 95(1):012413.

91. di Santo S, Burioni R, Vezzani A, Muñoz MA (2016) Self-Organized Bistability Associated with First-Order Phase Transitions. *Physical Review Letters* 116(24):240601.

92. Lundqvist M*, et al.* (2016) Gamma and Beta Bursts Underlie Working Memory. *Neuron* 90(1):152-164.

93. Engel AK, Fries P (2010) Beta-band oscillations—signalling the status quo? *Current Opinion in Neurobiology* 20(2):156-165.

94. Virkar Y, Clauset A (2014) POWER-LAW DISTRIBUTIONS IN BINNED EMPIRICAL DATA. *The Annals of Applied Statistics* 8(1):89-119.

95. Pritchard W (1992) *The Brain in Fractal Time: 1/F-Like Power Spectrum Scaling of the Human Electroencephalogram* pp 119-129.

96. Priesemann V, Valderrama M, Wibral M, Le Van Quyen M (2013) Neuronal Avalanches Differ from Wakefulness to Deep Sleep – Evidence from Intracranial Depth Recordings in Humans. *Plos Comput Biol* 9(3):e1002985.

97. Priesemann V, Munk MHJ, Wibral M (2009) Subsampling effects in neuronal avalanche distributions recorded in vivo. *BMC Neurosci* 10:40-40.

98. Chen Y-J, Papanikolaou S, Sethna J, Zapperi S, Durin G (2011) *Avalanche Spatial Structure and Multivariable Scaling Functions; Sizes, Heights, Widths, and Views through Windows* p 061103.

99. Wang S-J*, et al.* (2016) Stochastic Oscillation in Self-Organized Critical States of Small Systems: Sensitive Resting State in Neural Systems. *Physical Review Letters* 116(1):018101.

100. Benayoun M, Cowan JD, van Drongelen W, Wallace E (2010) Avalanches in a Stochastic Model of Spiking Neurons. *Plos Comput Biol* 6(7):e1000846.

101. Baldassarri A, Colaiori F, Castellano C (2003) Average Shape of a Fluctuation: Universality in Excursions of Stochastic Processes. *Physical Review Letters* 90(6):060601.

102. Poil S-S, van Ooyen A, Linkenkaer-Hansen K (2008) Avalanche dynamics of human brain oscillations: Relation to critical branching processes and temporal correlations. *Human Brain Mapping* 29(7):770-777.

103. Wang S-J, Hilgetag CC, Zhou C (2011) Sustained activity in hierarchical modular neural networks: self-organized criticality and oscillations. *Frontiers in computational neuroscience* 5:30-30.

104. Palva S, Palva JM (2018) Roles of Brain Criticality and Multiscale Oscillations in Temporal Predictions for Sensorimotor Processing. *Trends Neurosci* 41(10):729-743.

105. Hidalgo J*, et al.* (2014) Information-based fitness and the emergence of criticality in living systems. *P Natl Acad Sci USA* 111(28):10095-10100.

106. Uhlhaas Peter J, Singer W (2012) Neuronal Dynamics and Neuropsychiatric Disorders: Toward a Translational Paradigm for Dysfunctional Large-Scale Networks. *Neuron* 75(6):963-980.

107. Kaneko K (2018) Negative Symptoms and Cognitive Impairments in Schizophrenia: Two Key Symptoms Negatively Influencing Social Functioning. *Yonago Acta Medica* 61(2):091-102.

108. Kirkpatrick B, Fenton WS, Carpenter WT, Jr., Marder SR (2006) The NIMH-MATRICS consensus statement on negative symptoms. *Schizophrenia Bull* 32(2):214-219.

109. Geisler D*, et al.* (2015) Brain structure and function correlates of cognitive subtypes in schizophrenia. *Psychiatry Research: Neuroimaging* 234(1):74-83.

110. Hashimoto T*, et al.* (2003) Gene expression deficits in a subclass of GABA neurons in the prefrontal cortex of subjects with schizophrenia. *J Neurosci* 23(15):6315-6326.

111. Lau CG, Murthy VN (2012) Activity-Dependent Regulation of Inhibition via GAD67. *J Neurosci* 32(25):8521-8531.

112. McGrath J, Saha S, Chant D, Welham J (2008) Schizophrenia: A Concise Overview of Incidence, Prevalence, and Mortality. *Epidemiologic Reviews* 30(1):67-76.

113. V. Stewart C, Plenz D (2006) Inverted-U Profile of Dopamine–NMDA-Mediated Spontaneous Avalanche Recurrence in Superficial Layers of Rat Prefrontal Cortex. *The Journal of Neuroscience* 26(31):8148-8159.

114. Uhlhaas PJ, Singer W (2010) Abnormal neural oscillations and synchrony in schizophrenia. *Nat Rev Neurosci* 11:100.

115. Chalkiadaki K*, et al.* (2019) Development of the MAM model of schizophrenia in mice: Sex similarities and differences of hippocampal and prefrontal cortical function. *Neuropharmacology* 144:193-207.

116. Castane A, Santana N, Artigas F (2015) PCP-based mice models of schizophrenia: differential behavioral, neurochemical and cellular effects of acute and subchronic treatments. *Psychopharmacology* 232(21-22):4085-4097.

117. Mouri A, Noda Y, Enomoto T, Nabeshima T (2007) Phencyclidine animal models of schizophrenia: Approaches from abnormality of glutamatergic neurotransmission and neurodevelopment. *Neurochem Int* 51(2-4):173-184.

118. Hashimoto K*, et al.* (2003) Decreased Serum Levels of D-Serine in Patients With Schizophrenia: Evidence in Support of the N-Methyl-D-Aspartate Receptor Hypofunction Hypothesis of Schizophrenia. *JAMA Psychiatry* 60(6):572-576.

119. Andersen JD, Pouzet B (2004) Spatial memory deficits induced by perinatal treatment of rats with PCP and reversal effect of D-serine. *Neuropsychopharmacol* 29(6):1080-1090.

120. Fujita Y, Ishima T, Hashimoto K (2016) Supplementation with D-serine prevents the onset of cognitive deficits in adult offspring after maternal immune activation. *Sci Rep-Uk* 6.

121. Hattori R, Kuchibhotla KV, Froemke RC, Komiyama T (2017) Functions and dysfunctions of neocortical inhibitory neuron subtypes. *Nat Neurosci* 20(9):1199-1208.

122. Batista-Brito R*, et al.* (2017) Developmental Dysfunction of VIP Interneurons Impairs Cortical Circuits. *Neuron* 95(4):884-+.

123. Rudy B, Fishell G, Lee S, Hjerling-Leffler J (2011) Three Groups of Interneurons Account for Nearly 100% of Neocortical GABAergic Neurons. *Dev Neurobiol* 71(1):45-61.

124. Lewis DA, Hashimoto T, Mirnics K, Maldonado-Aviles JG, Morris HM (2005) Differential vulnerability of specific cortical GABA systems in schizophrenia. *Neuropsychopharmacol* 30:S3-S3.

125. Cho KKA*, et al.* (2015) Gamma rhythms link prefrontal interneuron dysfunction with cognitive inflexibility in Dlx5/6(+/-) mice. *Neuron* 85(6):1332-1343.

126. Verret L*, et al.* (2012) Inhibitory Interneuron Deficit Links Altered Network Activity and Cognitive Dysfunction in Alzheimer Model. *Cell* 149(3):708-721.

127. Goldey GJ*, et al.* (2014) Removable cranial windows for long-term imaging in awake mice. *Nat Protoc* 9(11):2515-2538.

128. Weichhart T*, et al.* (2010) The anti-inflammatory potency of dexamethasone is determined by the route of application in vivo. *Immunology Letters* 129(1):50-52.

129. Ennaceur A, Neave N, Aggleton JP (1997) Spontaneous object recognition and object location memory in rats: The effects of lesions in the cingulate cortices, the medial prefrontal cortex, the cingulum bundle and the fornix. *Exp Brain Res* 113(3):509-519.

130. Morrow BA, Roth RH, Elsworth JD (2000) TMT, a predator odor, elevates mesoprefrontal dopamine metabolic activity and disrupts short-term working memory in the rat. *Brain Research Bulletin* 52(6):519-523.

131. Horiguchi M, Meltzer HY (2013) Blonanserin reverses the phencyclidine (PCP)-induced impairment in novel object recognition (NOR) in rats: Role of indirect 5-HT1A partial agonism. *Behavioural Brain Research* 247:158-164.

132. Antunes M, Biala G (2012) The novel object recognition memory: neurobiology, test procedure, and its modifications. *Cogn Process* 13(2):93-110.

133. Deneux T*, et al.* (2016) Accurate spike estimation from noisy calcium signals for ultrafast three-dimensional imaging of large neuronal populations in vivo. *Nat Commun* 7:12190.

134. Bubenikova-Valesova V, Horacek J, Vrajova M, Hoschl C (2008) Models of schizophrenia in humans and animals based on inhibition of NMDA receptors. *Neurosci Biobehav R* 32(5):1014-1023.

135. Fagerholm ED, Dinov M, Knöpfel T, Leech R (2018) The characteristic patterns of neuronal avalanches in mice under anesthesia and at rest: An investigation using constrained artificial neural networks. *Plos One* 13(5):e0197893.

136. Ikonomidou C*, et al.* (1999) Blockade of NMDA receptors and apoptotic neurodegeneration in the developing brain. *Science* 283(5398):70-74.

137. Olney JW (1991) Excitotoxicity - Relevance to Brain Disorders in Both Youth and Old-Age. *Int Congr Ser* 968:765-768.

138. Olney JW*, et al.* (1991) Nmda Antagonist Neurotoxicity - Mechanism and Prevention. *Science* 254(5037):1515-1518.

139. Tome CML*, et al.* (2006) Neonatal exposure to MK801 induces structural reorganization of the central nervous system. *Neuroreport* 17(8):779-783.

140. Abekawa T, Ito K, Nakagawa S, Koyama T (2007) Prenatal exposure to an NMDA receptor antagonist, MK-801 reduces density of parvalbumin-immunoreactive GABAergic neurons in the medial prefrontal cortex and enhances phencyclidine-induced hyperlocomotion but not behavioral sensitization to methamphetamine in postpubertal rats. *Psychopharmacology* 192(3):303-316.

141. Lewis DA, Hashimoto T, Volk DW (2005) Cortical inhibitory neurons and schizophrenia. *Nat Rev Neurosci* 6(4):312-324.

142. Curley AA*, et al.* (2011) Cortical Deficits of Glutamic Acid Decarboxylase 67 Expression in Schizophrenia: Clinical, Protein, and Cell Type-Specific Features. *Am J Psychiat* 168(9):921-929.

143. Glausier JR, Lewis DA (2011) Selective Pyramidal Cell Reduction of GABA(A) Receptor alpha 1 Subunit Messenger RNA Expression in Schizophrenia. *Neuropsychopharmacol* 36(10):2103-2110.

144. Georgiev D*, et al.* (2014) Lower Gene Expression for KCNS3 Potassium Channel Subunit in Parvalbumin-Containing Neurons in the Prefrontal Cortex in Schizophrenia. *Am J Psychiat* 171(1):62-71.

145. Hu H, Martina M, Jonas P (2010) Dendritic Mechanisms Underlying Rapid Synaptic Activation of Fast-Spiking Hippocampal Interneurons. *Science* 327(5961):52-58.

146. Fish KN, Hoftman GD, Sheikh W, Kitchens M, Lewis DA (2013) Parvalbumin-Containing Chandelier and Basket Cell Boutons Have Distinctive Modes of Maturation in Monkey Prefrontal Cortex. *J Neurosci* 33(19):8352-8358.

147. Beneyto M, Morris HM, Rovensky KC, Lewis DA (2012) Lamina- and cell-specific alterations in cortical somatostatin receptor 2 mRNA expression in schizophrenia. *Neuropharmacology* 62(3):1598-1605.

148. Cichon J, Gan WB (2015) Branch-specific dendritic Ca2+ spikes cause persistent synaptic plasticity. *Nature* 520(7546):180-U180.

149. Karasawa J-i, Hashimoto K, Chaki S (2008) d-Serine and a glycine transporter inhibitor improve MK-801-induced cognitive deficits in a novel object recognition test in rats. *Behavioural Brain Research* 186(1):78-83.

150. Sagan C (1986) *Dragons of Eden: Speculations on the Evolution of Human Intelligence* (Ballantine Books).

151. Arcangelis Ld, Herrmann HJ (2013) Spontaneous neuronal activity as a self-organized critical phenomenon. *AIP Conference Proceedings* 1510(1):14-24.

152. Moretti P, Muñoz MA (2013) Griffiths phases and the stretching of criticality in brain networks. *Nat Commun* 4:2521.

153. Kuhn TS (1962) The Structure of Scientific Revolutions.

154. Gell-Mann M, Low FE (1954) Quantum Electrodynamics at Small Distances. *Physical Review* 95(5):1300-1312.

155. Mandelbrot B (1967) How Long Is the Coast of Britain? Statistical Self-Similarity and Fractional Dimension. *Science* 156(3775):636-638.

156. Penttonen M, Buzsáki G (2003) Natural logarithmic relationship between brain oscillators. *Thalamus & Related Systems* 2(2):145-152.